

# Interactive terrain visualization enables virtual field work during rapid scientific response to the 2010 Haiti earthquake

Eric Cowgill<sup>1,2\*</sup>, Tony S. Bernardin<sup>3</sup>, Michael E. Oskin<sup>1,2</sup>, Christopher Bowles<sup>1</sup>, M. Burak Yikilmaz<sup>1</sup>, Oliver Kreylos<sup>2,3</sup>, Austin J. Elliott<sup>1</sup>, Scott Bishop<sup>3</sup>, Ryan D. Gold<sup>4</sup>, Alexander Morelan<sup>1</sup>, Gerald W. Bawden<sup>5</sup>, Bernd Hamann<sup>2,3</sup>, Louise H. Kellogg<sup>1,2</sup>

<sup>1</sup>Department of Geology, University of California, Davis, California 95616, USA

<sup>2</sup>W. M. Keck Center for Active Visualization in the Earth Sciences, Department of Geology, University of California, Davis, California 95616, USA

<sup>3</sup>Institute for Data Analysis and Visualization, Department of Computer Science, University of California, Davis, California 95616, USA

<sup>4</sup>U.S. Geological Survey, Mail Stop 966, Denver, Colorado 80225, USA

<sup>5</sup>U.S. Geological Survey, 3020 State University Drive East, Modoc Hall Suite 4004, Sacramento, California 95819, USA

## ABSTRACT

The moment magnitude ( $M_w$ ) 7.0 12 January 2010 Haiti earthquake is the first major earthquake for which a large-footprint LiDAR (light detection and ranging) survey was acquired within several weeks of the event. Here we describe the use of virtual reality data visualization to analyze massive amounts (67 GB on disk) of multiresolution terrain data during the rapid scientific response to a major natural disaster. In particular, we describe a method for conducting virtual field work using both desktop computers and a 4-sided, 22 m<sup>3</sup> CAVE immersive virtual reality environment, along with KeckCAVES (Keck Center for Active Visualization in the Earth Sciences) software tools LiDAR Viewer, to analyze LiDAR point-cloud data, and Crusta, for 2.5 dimensional surficial geologic mapping on a bare-earth digital elevation model. This system enabled virtual field work that yielded remote observations of the topographic expression of active faulting within an ~75-km-long section of the eastern Enriquillo–Plantain Garden fault spanning the 2010 epicenter. Virtual field observations indicated that the geomorphic evidence of active faulting and ancient surface rupture varies along strike. Landform offsets of 6–50 m along the Enriquillo–Plantain Garden fault east of the 2010 epicenter and closest to Port-au-Prince attest to repeated recent surface-rupturing earthquakes there. In the west, the fault trace is well defined by displaced landforms, but it is

not as clear as in the east. The 2010 epicenter is within a transition zone between these sections that extends from Grand Goave in the west to Fayette in the east. Within this transition, between L'Acul (lat 72°40'W) and the Rouillone River (lat 72°35'W), the Enriquillo–Plantain Garden fault is undefined along an embayed low-relief range front, with little evidence of recent surface rupture. Based on the geometry of the eastern and western faults that show evidence of recent surface rupture, we propose that the 2010 event occurred within a stepover that appears to have served as a long-lived boundary between rupture segments, explaining the lack of 2010 surface rupture. This study demonstrates how virtual reality–based data visualization has the potential to transform rapid scientific response by enabling virtual field studies and real-time interactive analysis of massive terrain data sets.

## INTRODUCTION

The 12 January 2010 Haiti earthquake ended 240 years of relative quiescence following earthquakes that destroyed Port-au-Prince in 1751 and 1770. This was the deadliest earthquake of its size (moment magnitude,  $M_w$  7.0) in recorded history (Bilham, 2010), devastating the cities of Léogâne, Carrefour, and Port-au-Prince (Fig. 1). Starting 9 days after the earthquake, an area of ~850 km<sup>2</sup> was surveyed using airborne LiDAR (light detection and ranging) to support emergency response and damage assessment in urban areas as well to search for ground rupture (Fig. 1). These data were released as a bare-earth digital elevation model (DEM) and as a

classified (filtered) point cloud within a week of collection. Such rapid and open data collection and release serves as a model for future rapid response efforts (van Aardt et al., 2011).

The Haiti earthquake response survey is the first large-footprint LiDAR data set collected immediately after a major earthquake, foreshadowing the central role that such data are likely to play during rapid response to future natural disasters. The high spatial resolution (>3 points/m<sup>2</sup>), large spatial coverage (>100 km<sup>2</sup>), and ability to image through vegetation canopy make airborne LiDAR data particularly useful for determining overall fault geometry (DeLong et al., 2010; Frankel et al., 2007a, 2007b; Frankel and Dolan, 2007; Haugerud et al., 2003; Hilley et al., 2010; Oskin et al., 2007a, 2007b), identifying and reconstructing offsets produced during coseismic surface rupture (Haugerud et al., 2003; Oskin et al., 2012; Zielke et al., 2010), and supporting field investigations during rapid scientific response (Prentice et al., 2010). The growing importance of LiDAR data in understanding surface rupture was also indicated by the collection of LiDAR data shortly after the 4 April 2010  $M_w$  7.2 El Mayor–Cucapah earthquake in Mexico (Oskin et al., 2012) and the 4 September 2010  $M_w$  7.1 Darfield (Canterbury) earthquake in New Zealand (Quigley et al., 2012). For example, the Darfield data were collected six days after the earthquake and were used to map the main features of the rupture and both cross-check and augment field measurements used to determine the slip function for the rupture (Quigley et al., 2012). However, despite their utility, LiDAR data also pose significant computational challenges for visualization and analysis. Such challenges are particularly acute

\*Corresponding author: escowgill@ucdavis.edu



**Figure 1.** (A) Plate-boundary context of the eastern Enriquillo fault zone. (B) 2010 epicenter and LiDAR (light detection and ranging) coverage. Place names are from 1:50,000 scale topographic maps (U.S. Army Map Service, 1962, 1988, 1991a, 1991b) and Google Earth.

in the context of time-sensitive rapid scientific response efforts. For example, the total Haiti LiDAR data set contained  $\sim 2.9 \times 10^9$  individual point-measurements in three-dimensional (3D) space of surface topography at an average density of 2 points/m<sup>2</sup> over urban areas and 5 points/m<sup>2</sup> along the Enriquillo–Plantain Garden fault (EPGF) (van Aardt et al., 2011; <http://www.opentopography.org/index.php/about/datasets/metrics>). As such, these data posed an unprecedented opportunity and challenge in terms of rapid data analysis.

This paper has three goals: describe and evaluate a method for virtual reality–based analysis

of LiDAR data during rapid scientific response to a major natural disaster; report observations made using this method regarding the geometry and the activity of the EPGF in the vicinity of the 2010 epicenter and explore their implications for the earthquake behavior of the fault; and use this experience to inform future rapid scientific response efforts.

The LiDAR data analyzed here were acquired 21–27 January 2010 by the Rochester Institute of Technology (Rochester, New York) and Kucera International, under subcontract to ImageCat Inc. and funded by the Global Facility for Disaster Reduction and Recovery, hosted at

The World Bank. The U.S. Geological Survey coordinated expansion of the surveys to encompass the Enriquillo fault south of Port-au-Prince from L'Acul to Lago Enriquillo, with the exception of a 4 km section of fault east of Pétionville that was not imaged (Fig. 1). Classification of the data to produce a bare-earth DEM was conducted by the Information Products Laboratory for Emergency Response (<http://ipler.cis.rut.edu/>), with emphasis on rapid turnaround (van Aardt et al., 2011). Airborne LiDAR data were also collected by the U.S. military using the ALIRT (Airborne Ladar Imaging Research Testbed) system, but the data had minimal fault coverage.

We analyzed the Haiti LiDAR data using a CAVE immersive virtual reality environment and software tools developed by the W.M. Keck Center for Active Visualization in the Earth Sciences (KeckCAVES, [www.keckcaves.org](http://www.keckcaves.org)). The approach reported here used LiDAR and other terrain data to create virtual scaled models of the landscape that geologists visited remotely to conduct virtual field work. These models contained the topographic measurements at their full resolution and were built from the cloud of LiDAR point measurements and DEMs interpolated from those data. This method complements field measurements by allowing the observer to move quickly through terrain data, view areas of interest from any perspective, project and measure offset landforms, and record observations directly on the virtual landscape. Because a main goal of this study was to explore the use of virtual reality–based data analysis during rapid response, we also studied and quantified the performance, speed, and accuracy of key aspects of the method. Thus, this paper describes both the performance of the visualization approach and the observations it allowed us to make that have bearing upon the earthquake behavior of the EPGF.

We used this system to observe fault geometry, fault segmentation, and evidence of past surface rupture along the  $\sim 75$ -km-long portion of EPGF imaged by the 2010 LiDAR data. Although the basic geometry and plate-boundary context of the EPGF were well established prior to the 2010 earthquake, the detailed geometry of the fault in the vicinity of the 2010 epicenter had not been reported. Establishing such fault geometry and segmentation is important because they influence the extent and style of coseismic fault rupture and thus earthquake size (Duan and Oglesby, 2006; King and Nabelek, 1985; Lozos et al., 2011; Oglesby, 2005; Segall and Pollard, 1980; Stein, 1999; Wesnousky, 1988, 2006). Determining fault geometry is also important for supporting sustainable reconstruction in Haiti (Lerner-Lam, 2010) and under-

standing the complex deformational processes occurring along the northern boundary of the Caribbean plate (Mann et al., 2002).

The 2010 Haiti earthquake provided an important venue in which to develop methods for remote, virtual reality–based data analysis due to the unprecedented availability of post-event LiDAR measurements and other remote sensing data that were collected or released in the days and weeks immediately following the event. Because no surface rupture has been observed for the 2010 earthquake (Calais et al., 2002; Hayes et al., 2010; Koehler and Mann, 2011; Prentice et al., 2010), this event does not provide the opportunity to evaluate the utility of such remote methods for the rapid discovery and documentation of surface rupture. However, aspects of the visualization system were used as part of the analysis of the surface rupture that was produced by the Sierra El Mayor–Cucapah earthquake and that was imaged using both ground-based and airborne LiDAR data. We used this experience to augment our evaluation of the virtual reality method.

## GEOLOGIC SETTING

The EPGF is a 1200-km-long transform system within the complex Caribbean–North American plate boundary zone (Mann et al., 2002, 1995) (Fig. 1). On Hispanola, this transform system separates the Caribbean plate to the south from the Gonâve microplate to the north (Mann et al., 2002, 1995). Slip inversion, patterns of coastal deformation, and geodetic data indicate that the 2010 event resulted from an ~35–40-km-long westward rupture on a fault array associated with the EPGF, but not the strike-slip fault (Calais et al., 2010; Hayes et al., 2010).

Mann et al. (1995) used geological mapping, air photo analysis, and seismic reflection data to establish the regional continuity and geometry of the EPGF, document Quaternary faulting, and show that the fault coincides with prominent, east-west–trending linear valleys along the Momance and Froide Rivers (Figs. 1 and 2). Along strike to the west, the EPGF is punctuated by extensional fault stepovers and bends at Miragoâne Lake and Clonard, and a restraining bend at Pic Macaya (Mann et al., 1995). Total offset along the EPGF is estimated to be 30–50 km (Mann et al., 1995), although the piercing relations are poorly defined.

Historical records document a cluster of large earthquakes in southwestern Haiti in the eighteenth and nineteenth centuries (Dolan et al., 1998; Mann et al., 1998, 1995; McCann, 2006; Scherer, 1912), with events on 18 October and 21 November 1751; 3 June 1770; and 8 April 1860 (Scherer, 1912). Both the November 1751

and June 1770 events destroyed Port-au-Prince, although the city only had 100 and 683 houses in 1751 and 1764, respectively (Scherer, 1912). The distribution of reported damage for these earthquakes suggests that they were produced by rupture within the EPGF. However, prior studies lack consensus regarding the placement and extent of these ruptures along the fault. Although most published maps show the November 1751 event east of the 1770 event, the absolute positions of each rupture shift along fault strike among various reports; some (Ali et al., 2008; Calais et al., 2010; Manaker et al., 2008) locate the events farther west than others (Bakun et al., 2012; Dolan et al., 1998; Mann et al., 2002, 1995; McCann, 2006; Prentice et al., 2010). New analysis of historical damage reports indicates that the 1770 and November 1751 events were west and east, respectively, of the 2010 earthquake (Bakun et al., 2012). Slip on structures other than the EPGF may also explain one or more of these events.

Neither observation from paleoseismic trenching nor Quaternary geologic slip rates have been reported for the EPGF. Based on elastic-dislocation modeling of global positioning system (GPS) measurements made prior to the 2010 earthquake, Manaker et al. (2008) reported a geodetic slip rate along the EPGF of  $7 \pm 2$  mm/yr. Likewise, Calais et al. (2010) modeled a rate of  $5\text{--}6 \pm 2$  mm/yr on the southern peninsula fault zone. Manaker et al. (2008) estimated that the EPGF south of Port-au-Prince has the potential to rupture with ~2 m of displacement to produce an M 7.2 earthquake by assuming that the fault last ruptured in 1751, and has subsequently been fully locked and steadily loaded at the geodetic rate. An earthquake of such magnitude implies rupture of a fault patch ~100 km long and ~12 km deep.

## METHODS

The approach described here exploits the human capacity for visually identifying meaningful patterns embedded in noisy data by using immersive, interactive data visualization in real time. Here, immersive means that users see, and are surrounded by, a virtual scaled model of the data; interactive means that users immediately see the results of operations they perform on those data without waiting for the view to refresh; and real time means the display updates at the minimum rate of 50 frames/s needed to support interactive stereoscopic rendering (Kreylos et al., 2003). The system we have developed to support this approach incorporates both hardware and software that together create a virtual landscape that allows remote users to make many observations of landform geom-

etry that have previously required field work. This system is designed to generate the experience of spatial presence, in which users believe they are physically located within a mediated environment (e.g., a projected display of a terrain data set) rather than in their true physical location (e.g., in a laboratory) (IJsselstein et al., 2000; Lombard and Ditton, 1997; Minski, 1980; Steuer, 1995; Wirth et al., 2007; Witmer and Singer, 1998). McGreevy (1992) investigated presence during field geology and found that tools enabling user-directed exploration, such as those described here, are required to support remote geological investigation.

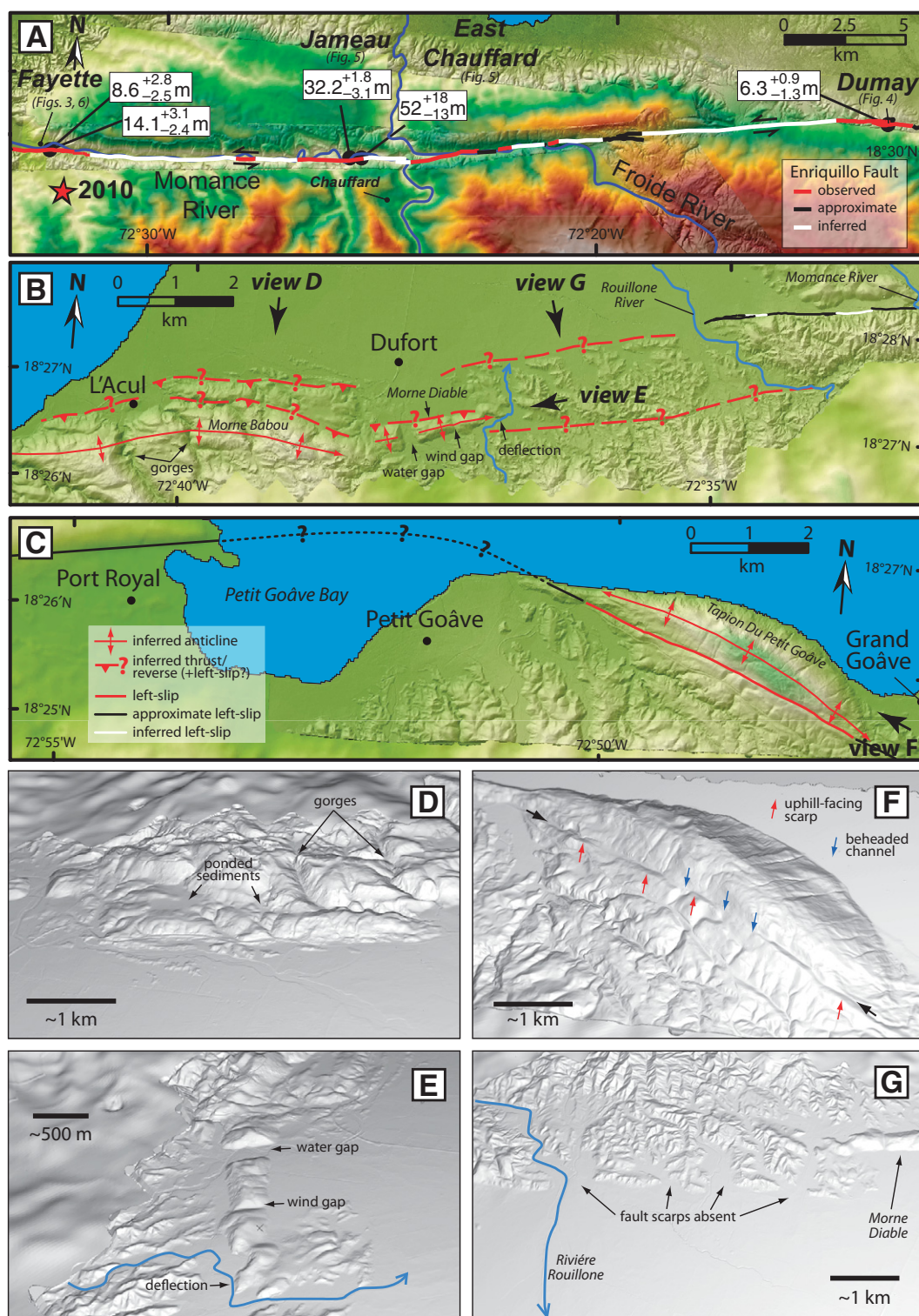
## Hardware

The KeckCAVES immersive visualization environment is a 22 m<sup>3</sup>, 4-sided MechDyne CAVE with projection on 3 walls (front and 2 sides) and the floor, each of which is 3 × 2.4 m. Stereoscopic images are projected onto all four surfaces using one three-chip DLP (digital light processing) projector (Christie Mirage S+4K) for each. Within CAVE environments, the user perceives a seamless 3D environment that can be explored (Cruz-Neira et al., 1992). In the case of LiDAR data, this environment renders the data as a scaled model of the landscape. An Intersense IS-900 wireless tracking system synchronizes the display with the 3D position and orientation of the user's head, so that the user maintains the sense of spatial presence. Using a position-tracked, six-button hand-held wand, users interact with the virtual landscape by grabbing, rotating, and panning through the terrain data, selecting points for manual data classification or measurement of local surface orientation, measuring landform offsets, or recording observations using standard annotated geologic map symbols draped on the terrain. The head-tracked stereoscopic 3D display and wide field of view enhance depth perception, enabling rapid identification of structures in 3D space that are present in LiDAR point clouds. Immersive visualization (in this case high-resolution stereoscopic images with a large field of view) and real-time interaction are important in generating the experience of spatial presence (e.g., Lombard and Ditton, 1997; Steuer, 1995).

## Software

Use of the CAVE hardware as an analytical device was enabled by two free, open-source software tools: LiDAR Viewer (Kreylos et al., 2008) and Crusta (Bernardin et al., 2011). Both applications run on Macintosh and Unix platforms using the Vrui (Virtual Reality User Interface) development toolkit (Kreylos, 2008).

Figure 2. Results of remote mapping of the Enriquillo–Plantain Garden fault zone. (A) Eastern reach. Mapping shows late Quaternary surface rupture expressed as scarps and offset landforms that were remotely documented and measured in this study (Figs. 4–6). (B) Transitional reach. (C) Western reach. (See Fig. 1B for locations.) (D) Perspective view (i.e., virtual field photograph) as seen in Crusta software of the first-released bare-earth LiDAR (light detection and ranging) digital elevation model (DEM) (1 m/pixel) merged with ASTER (Advanced Spaceborne Thermal Emission and Reflection Radiometer) DEM (30 m/pixel). Scale bar is approximate for image center. View is to south showing range front at Morne Babou. The linear range front, stepped increase in elevation, gorges from probable antecedent streams, and ponded sediments all suggest that this area is underlain by a south-dipping thrust/reverse system. (E) Perspective view (i.e., virtual field photographs; see description in D) to west along strike of Morne Diabie, showing water and wind gaps and a deflected drainage indicating that the ridge is an actively growing fold. (F) Perspective view (i.e., virtual field photographs; see description in D) to northwest of Tapion Du Petit Goâve showing active fault trace (black arrows) defined by uphill-facing scarps (red arrows) and beheaded channels (blue arrows). The beheaded channels suggest a component of strike slip along the fault. (G) Perspective view (i.e., virtual field photograph; see description in D) to south of low-relief and embayed mountain front between Rouillone River and Morne Diabie shows no clear fault trace despite high potential for scarp preservation in the alluvial fans. Although the fault appears to be both onshore and offshore between L'Acul and Port Royal, our observations are limited to onshore areas because we did not have high-resolution bathymetric data to merge with the LiDAR data at the time of analysis. Such data have subsequently revealed faults offshore (Hornbach et al., 2010).



(Both applications are available from <http://keckcaves.org/software/>.) Because applications using the Vrui toolkit are written without a particular input environment in mind, we used LiDAR Viewer and Crusta on multiple different hardware environments including standard desktop computers, a 3D display, and the CAVE fully immersive visualization environment. Both LiDAR Viewer and Crusta employ highly efficient approaches to data handling and rendering such as hierarchical data structures and view-dependent, multiresolution, out-of-core rendering. This means that the applications only load those parts of a data set that are within a user's current view and then only render the visible parts of the data at the resolution supported by the hardware. As a result, data sets many times larger than the computer's main memory can be visualized and interactively manipulated.

LiDAR Viewer is an immersive application for real-time visualization of multibillion-point LiDAR point clouds without subsampling or reduction in data size (Animation 1).

Interactive visualization of LiDAR point measurements differs from most prior work, which focused primarily on analysis of DEMs derived from the scattered LiDAR measurements by interpolation and gridding. However, a similar approach to visualizing LiDAR point clouds using point-based rendering has also been reported (Kovač and Žalik, 2010). In LiDAR Viewer, point data are preprocessed and organized into an octree structure to provide a multiscale representation and efficient localized point data retrieval, which enables seamless real-time visualization of arbitrarily large data sets. The octree data structure makes it computationally feasible to use a point set comparison tool to identify common points within two different versions of the same point cloud, such as a filtered cloud containing only bare-earth returns and the full cloud from which it was derived. LiDAR Viewer supports real-time navigation; real-time interactive illumination of the point cloud using multiple light sources at arbitrary positions; point selection and extraction for further processing; fitting of geometric primitives (plane, sphere, cylinder) to selected points; visualization of point distances from a plane; and extraction of profile curves. The illumination functions support dynamic shading of the point cloud; this enables feature recognition by creating hill-shade images directly from the cloud that better convey surface shape than illumination by return intensity alone. Support for this feature is integrated into the preprocessing stage: for each point we compute its normal direction to be the same as the one of the best-fit plane to the neighboring points within a user-defined radius. By enabling such interactive



**Animation 1.** This movie demonstrates both visualization of the Haiti point-cloud data and results of both automatic and manual filtering using LiDAR Viewer. The movie is in MPEG-4 format and can be viewed with QuickTime software (<http://www.apple.com/quicktime/download>) from Apple. If you are viewing the PDF of this paper or reading it offline, please visit <http://dx.doi.org/10.1130/GES00687.S1> or the full-text article on [www.gsapubs.org](http://www.gsapubs.org) to view Animation 1.

analysis of LiDAR data, LiDAR Viewer contrasts with approaches emphasizing automated algorithmic feature extraction (e.g., Filin, 2004; Keller et al., 2011a, 2011b).

Crusta (Bernardin et al., 2011) is an immersive virtual globe that accurately renders in real time DEM and image data with both large coverage (e.g., whole earth) and high resolution (e.g., submeter) while minimizing the performance requirements of the computer's graphics subsystem (Animation 2). To provide near-uniform and isotropic resolution everywhere on the sphere, Crusta represents the globe as a 30-sided polyhedron, each face of which is delineated by 4 great-circle segments. The resulting identical parallelograms can be repeatedly subdivided to represent topographic or image data at arbitrarily high resolution. Crusta enables data exploration and feature discovery by supporting dynamic manipulation of the visualization such as interactive surface shading, real-time scaling of vertical exaggeration, and hardware-accelerated interactive manipulation of the texture color palette. A particular application of the dynamic color mapping is the generation of textured isolines representing topographic contour lines that can be moved across the terrain to investigate topographic details such as the geometry of an alluvial fan or a fault scarp. Topographic features, such as fault scarps or landforms displaced by coseismic surface rupture, can be documented by directly mapping on the virtual landscape using standard geographic information system (GIS) formats (e.g., shapefiles, kml).



**Animation 2.** This movie both explains the key geometric features found at the Dumay site and demonstrates interactive mapping there using the virtual globe application Crusta. The movie is in MPEG-4 format and can be viewed with QuickTime software (<http://www.apple.com/quicktime/download>) from Apple. If you are viewing the PDF of this paper or reading it offline, please visit <http://dx.doi.org/10.1130/GES00687.S2> or the full-text article on [www.gsapubs.org](http://www.gsapubs.org) to view Animation 2.

### Visualization of Filtered Point Cloud

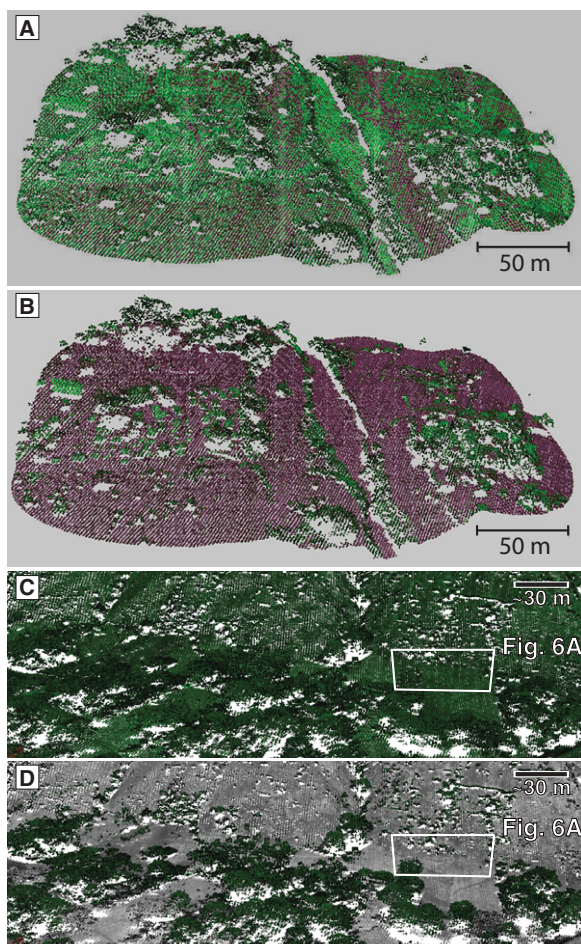
Bare-earth DEMs are typically generated from LiDAR point clouds using an automated filtering algorithm. This approach uses local gradients between points to classify returns as vegetation, building, or other non-ground points (e.g., Haugerud et al., 2003). As a result, automated filtering can produce a loss of spatial resolution by erroneously removing ground returns in areas of steep terrain, high local relief, or where overlapping scans show small vertical offsets due to errors in scan coregistration. An aggressive automated scheme is most appropriate for settings with low relief and high density of buildings (such as cities), while other approaches are more appropriate for settings in which high local relief is part of the signal being sought, such as the search for young fault scarps.

For the Haiti data set, we visualized the results of the automated filtering by using a point set subtraction tool in LiDAR Viewer to subtract the bare-earth points from the full cloud to obtain the set of points discarded during generation of the bare-earth DEM. We then generated a LiDAR Viewer project with the bare-earth points in one color and the discarded points in another and visualized the result in the CAVE to determine whether points in the ground plane had been removed (Animation 1; Fig. 3A).

### Manual Filtering

To enable accurate mapping and measurement of individual landform offsets, we manually classified the point cloud in select areas to maximize the number of ground returns in

**Figure 3. Manual classification of vegetation points resulted in improved data density, as illustrated by pairs of screen shots from LiDAR Viewer (see text) comparing automated (A, C) and manual (B, D) classifications at the Dumay (A and B) and Fayette (C and D) sites. Points classified as vegetation are green and those in the bare-earth class are either purple or gray. In the automated classification, ~90% of the points are green, with visualization in the CAVE (see text) revealing many misclassifications. We restored these misclassified points by manually filtering the data using LiDAR Viewer and the CAVE, and found that only ~30% of the points were vegetation. See text and Animation 1 for point-cloud visualization and explanation of manual classification.**



the bare-earth model and thereby increase the resolution of the bare-earth DEM (Figs. 2A and 3). During manual classification, a virtual paintbrush selection tool was used to first manually extract a subset of the full point cloud in an area 0.016–0.12 km<sup>2</sup> around each site of interest. This same tool was then used to manually isolate bare-ground returns by interactively selecting non-ground returns (e.g., trees, bushes, buildings) for removal (Animation 1). Manually classified clouds were then gridded at 0.5 m/pixel using Kriging in ArcGIS 9.3 (<http://www.esri.com>).

### Remote Mapping

For regional mapping, we observed and documented fault-zone morphology by using Crusta to visualize and map directly on the first-released bare-earth LiDAR DEM. Animation 2 demonstrates this approach in a CAVE immersive environment. To map, we used a 2.5 GHz Intel Core 2 Duo MacBook Pro laptop computer with 2 GB of 667 MHz DDR2 SDRAM. At specific sites of interest along the EPGF we studied landform geometries using both desktop and

CAVE environments, the unfiltered point cloud, and bare-earth DEMs derived from automated and manual vegetation filtering. We then made detailed neotectonic maps and offset measurements at three of the sites using the same laptop.

To evaluate the utility of our method for virtual reality-based remote data analysis, we worked independently from, and concurrently with, a field-based investigation reported by Prentice et al. (2010) and other studies of the earthquake (Calais et al., 2010; Hayes et al., 2010; Hornbach et al., 2010). To avoid biasing our site measurements, and to allow us to evaluate the accuracy of our remote methods, we identified, mapped, and measured sites (described in the following) before comparing our remote measurements to those made in the field.

### Offset Measurement

To measure offsets and associated uncertainties in the virtual landscape, we fit piercing lines to offset landforms both north and south of the fault and then projected these lines into the fault trace. To quantify offset uncertainty, we considered different projections fit to both segments

of the faulted landform, and then made repeat measurements of the offsets for these different projections. Offsets reported here are our best measurement of the simplest projection. The associated uncertainties encapsulate the range of maximum and minimum offsets obtained using different projections and repeat measurements.

Our measurement approach replicated the process used to measure landform offsets in field-based studies (e.g., see Fig. 3 of Gold et al., 2011). To determine riser offsets in the field, a geologist measured the riser trends using a geologic compass, projected the riser crests into the fault zone along these bearings to estimate piercing-point locations, and then measured the lateral offset between these points using a tape measure. The field observations we report were made by one of us (Ryan Gold) during work by a U.S. Geological Survey field party. Summary compilations of field observations by this group were reported in Prentice et al. (2010) and Hayes et al. (2010), including some by Ryan Gold (also reported here).

## RESULTS

In this section we report on both the performance of the virtual reality-based visualization approach and the neotectonic observations it yielded.

### Rapid Data Exploration

For both bare-earth DEMs and the point cloud, it took less than 24 h to download and preprocess data and begin making remote observations using the virtual reality-based visualization method. The slowest step was downloading the data. On 4 February 2010 we obtained access to the DEM data, downloaded and preprocessed them for Crusta, and began analysis. To create the Crusta project, we merged DEMs of differing resolutions: 1 m/pixel in the 850 km<sup>2</sup> area covered by the bare-earth LiDAR DEM (7 GB on disk), 30 m/pixel from ASTER (Advanced Spaceborne Thermal Emission and Reflection Radiometer) DEM data over the remainder of Hispaniola, and 500 m/pixel from Blue Marble next generation data (<http://earthobservatory.nasa.gov/Features/BlueMarble>; Stockli et al., 2006) over the remainder of the globe for spatial reference. Mosaicking and preprocessing produced a 9.32 GB database and took 110 min on a 2.93 GHz Quad-Core Intel Xeon Mac Pro desktop computer with 3 GB of 1066 MHz DDR3 RAM. We learned the point cloud was available in the evening of 9 February 2010 and began analysis with LiDAR Viewer the following day. We constructed two composite point clouds by merging individual tiles (obtained from [6](http://</a></p>
</div>
<div data-bbox=)

was [ftp.cis.rit.edu/LiDAR\\_LAS\\_Files/](http://ftp.cis.rit.edu/LiDAR_LAS_Files/)). One data set included only the bare-earth points as originally classified in the data served by the Rochester Institute of Technology (331,053,823 points, 8.71 GB on disk). The second contained the full point cloud (2,700,563,734 points, 66.8 GB on disk). Merging and octree preprocessing took 30 min for the bare-earth points and 230 min for the full cloud using the desktop machine described herein. The total number of LiDAR returns for the data we analyzed differs by 5% from those listed at OpenTopography (i.e., 2,853,027,995 returns, 78.3 GB on disk; <http://www.opentopography.org/index.php/about/datasetsmetrics>).

The virtual reality-based visualization system enabled rapid exploration by allowing real-time interactive visualization of both the DEM and point-cloud data at their full spatial extent and resolution along the ~75-km-long section of the EPGF imaged by LiDAR (e.g., Animation 1). This exploration showed no evidence of 2010 surface rupture, consistent with simultaneous field observations (Bilham, 2010; Prentice et al., 2010). However, it did reveal the overall fault geometry (Fig. 2) and evidence of older surface rupture at four sites (Dumay, Jameau, East Chauffard, and Fayette), including landform offsets as small as 5–10 m. These observations are reported in the following.

The visualization system also allowed operations that are not possible in the field. Dynamic manipulation of the illumination direction using a virtual spotlight allowed us to more clearly see the geometry of the fault trace and offset landforms (e.g., Animation 2). Likewise, the system made it possible to move between sites tens of kilometers apart within a few seconds, record observations as linework drawn on the landscape while simultaneously manipulating the point of view, look at the terrain from within the Earth to rapidly identify channel thalwegs obscured from above by vegetation, and vertically exaggerate the topography by factors of 5–15 to identify slope breaks.

### Evaluation of Automated Filtering

Using the visualization system, we found that the original bare-earth DEM was produced using an aggressive classification scheme that performed poorly in the steep terrain along the Enriquillo fault. As a result, the original bare-earth DEM lacked topographic detail relative to other 1 m DEMs from airborne LiDAR with similar point densities, such as those along the northern San Andreas fault in California (e.g., 1.8 points/m<sup>2</sup> for 2003 NASA and U.S. Geological Survey or 5 points/m<sup>2</sup> for 2007 EarthScope data sets). Initial visual comparison of the topog-

raphy of the fault trace imaged in the unclassified point cloud with its representation in the original bare-earth DEM indicated that topographic details evident in the full cloud were absent from the DEM. Using the point set comparison tool in LiDAR Viewer, we quantified the number of points removed during automated classification by comparing the full and bare-earth classified point clouds, and found that 88% of the points had been identified as non-ground returns in the original classification. Removal of these points reduced the average point density for the data set as a whole from 3.2 to 0.4 points/m<sup>2</sup>, meaning the initial 1 m resolution DEM was generated by gridding a small subsampling of the original data, with <1 elevation measurement/cell. Most of the point cloud covers areas that are heavily urbanized. Point set comparisons for rural areas along the EPGF had equivalent levels (91%) of point removal. Visualization of the filtered point cloud in the CAVE indicated that numerous ground returns had been misclassified as vegetation points (Animation 1), which we determined by placing the ground plane at eye level and then moving along this surface.

We conclude that the initial vegetation filtering, conducted within days of data collection to enable quick release of the results and support relief efforts (van Aardt et al., 2011), used an aggressive classification scheme to produce the bare-earth DEM. Based on the frequency of points misclassified as vegetation, we infer that this classification used a very low point-to-point threshold angle to identify the bare earth. While appropriate in low-relief urban regions primarily targeted by the survey, this scheme performed poorly in the steep terrain along the EPGF. Reprocessing several 1 km<sup>2</sup> patches of data with a less aggressive automated scheme classified 64% of the points as non-ground returns, with numerous misclassifications still evident.

### Manual Filtering

Manual classification took several hours per site and removed ~30% of the points, thereby increasing the local point density relative to the original classification from 0.5 to 3.5 points/m<sup>2</sup>. All sites were all on the EPGF, where original point densities were higher (5 points/m<sup>2</sup>) than for the data set as a whole (3.2 points/m<sup>2</sup>) due to the lower density of data over urban areas (2 points/m<sup>2</sup>) (van Aardt et al., 2011). It is important that manual classification selectively removed all vegetation and/or building points, leaving the points in the ground plane at their full original point density, not just a higher average point density. The bare-earth DEMs derived from the manually filtered cloud have more topographic details than those generated from

automated processing, as shown in Animation 1. Manual classification increased the DEM resolution from 1 m<sup>2</sup> to 0.5 m<sup>2</sup> at 4 sites of interest and improved the ability to remotely observe, document, and measure the landform offsets.

We found that manual classification was not feasible on a standard desktop computer because the lack of depth perception made it difficult to both identify and select non-ground returns. However, classification was straightforward in the CAVE; the stereoscopic display allowed users to easily recognize and select structures because the system allowed them to see the relative positions of points when the cloud was stationary and there was no motion parallax. Reproducibility tests on a similar data set indicated that results of such manual classification are generally very similar when performed by different users, although one analyst was particularly aggressive in classifying points as vegetation (Bowles, 2009). We found that manual classification was useful when it was necessary to rapidly classify data in small areas while preserving the most bare-ground returns. Although manual classification using LiDAR Viewer avoids the licensing and training expenses required to use commercial packages (e.g., TerraScan; <http://www.terrasolid.fi/en/products/terrascan>), we suspect that it is not cost effective for areas >1 km<sup>2</sup> due to the time required to manually identify and select large numbers of non-ground returns.

### Regional Fault Geometry

The visualization system allowed us to remotely observe tectonic landforms, range-front morphology, and overall fault geometry using the first-released bare-earth LiDAR DEM. These remote observations indicated that geomorphic evidence of active faulting within the EPGF is clearer east of the 2010 epicenter than to the west, and that these two fault sections are separated between Grand Goâve and Fayette by a transition zone in both fault geometry and the expression and style of active deformation (Figs. 1 and 2). The following section reports our observations proceeding from Dumay in the east to Port Royal in the west (Figs. 1 and 2).

#### Eastern Reach

The eastern fault reach is between Dumay and Fayette, east of the 2010 epicenter, and preserves abundant evidence of prior surface-rupturing earthquakes. Regionally, this section of the EPGF is defined by a linear set of fault traces trending N82°E for >35 km (Fig. 2A). Between Dumay and Fermate, the trace is defined by sag ponds and uphill-facing scarps, although it is obscured by urbanization south of Pétienville. Between

Fayette and Fermate, the EPGF coincides with linear valleys along the north-northwest-flowing Froide and Momance Rivers, which deflect left laterally along the fault for ~7 km and ~14.5 km, respectively. Mann et al. (1995) noted the prominent fault trace and river deflections along these valleys. The topographic expression of the fault has been obliterated where it crosses the active river channels, but the fault is well defined by uphill-facing scarps, sidehill benches, and deflections in incised tributary channels where it crosses meander loops along the Momance River and fluvial terraces within both river valleys. Detailed maps and measurements of offset landforms are reported herein for four sites along the eastern fault section.

### Transition

A transition in both range-front geometry and the expression and style of active deformation occurs between Fayette in the east and Grand Goâve in the west (Fig. 2). The east end of this transition roughly coincides with the 2010 epicenter. Within the transition, the Léogâne fan at the mouth of the Momance and Rouillone Rivers depositionally abuts mountainous topography to the south, with minimal evidence of recent faulting. Between these rivers, the range front is ~4 km north of the front to the west and is crossed by an ~3-km-long, N82°E trending linear valley that is oblique to the regional drainage direction. This valley is aligned eastward across a saddle with the Momance River valley and the main trace of the EPGF.

Between the Rouillone River and Dufort, the range front trends ~N73°E with a markedly different topographic expression than other sections of the EPGF that we observed. Here, a 2-km-wide belt of low-relief foothills is between the main range to the south and the Léogâne fan to the north. The northern edge of these foothills is poorly delineated due to low relief and extensive embayment (Fig. 2B), and we found no clear, throughgoing fault trace along this range front.

Between Dufort and L'Acul, the range front is defined by a 100–200-m-high escarpment that is cut by a series of gorges lacking well-developed tributary networks 1–2 km upstream from the range front. Interfluvies between these gorges are low-relief uplands of similar elevation. Within this area, at Morne Babou, the range front trends east-west and is stepped, with a linear ridge of intermediate-elevation topography paralleling the range front and separating the main range to the south from the fan to the north. Sediment from channels draining the main range appears ponded on top of this intervening ridge (Fig. 2D). Likewise, at Morne Diable, ~1 km south-east of Dufort, a smaller (2 km long) linear ridge

trends N71°E and is ~70 m above the Léogâne fan to the north. This ridge is crossed by a north-flowing river at its western end, is cut by a dry valley orthogonal to the long axis of the ridge to the east, and deflects a northwest-flowing stream by ~90° at the eastern end of the ridge. Between L'Acul and Grand Goâve, the range front curves ~30° until it trends N62°E to define a roughly linear section of coastline.

### Western Reach

The western section is west of Grand Goâve; our observations here were limited due to the lack of LiDAR data along the fault west of Port Royal. This reach is characterized by tectonic ridges at Tapion Du Petit Goâve and north of Port Royal (Figs. 2C, 2F). Tapion Du Petit Goâve is an elongated, N65°W trending ridge that is ~400 m high, ~5 km long, and ~2 km wide. This ridge is bound to the northeast by the ocean and to the southwest by mountainous topography that is both more deeply dissected and lower elevation than the ridge. A clearly active fault trace with uphill-facing scarps, sidehill benches, and beheaded channels is on the southwestern flank of the ridge and trends N67°W (Fig. 2F). The ridge crest plunges symmetrically to the northwest and southeast and the fault trace dies out in both directions.

North of Port Royal (Fig. 2C), the EPGF is defined by a linear, N78°E trending ridge that is ~5 km long and ~300 m high, with a steep southeastern face dissected by linear channels. The ridge projects offshore to the east across the mouth of Petit Goâve Bay. The elevation of the ridge and the degree of dissection along the southeastern face decrease from west to east.

### Landform Offsets

The following summaries of our remote observations at four sites along the EPGZ demonstrate that virtual reality visualization enabled us to characterize fault geometry at a level of detail approaching that typically obtained by field studies during rapid response. In two cases for which comparison with independent field observations was possible (Dumay and Jameau), the remote mapping identified key relationships that were also seen in the field, with both remote and field-based offset measurements being equivalent within error (Table 1).

### Dumay

The Dumay site (Figs. 2A and 4) is located where the EPGF crosses a north-flowing tributary to the Grise River. We identified and mapped the site remotely (Animation 2). Remote observations indicated a single topographically expressed fault trace crossing a gently north sloping and agricul-

turally modified alluvial fan (T2), the surface of which is incised ~20 m by a modern channel (T0). Along the west bank of the T0 channel, an inset terrace (T1) is ~10 m below the T2 surface. A northeast-facing fluvial terrace riser separates the T2 and T1 surfaces and is steepest at the crest and heavily vegetated. The fault is clearly defined on the west bank by a tectonic furrow and two uphill-facing scarps on T2. The furrow and lower of the two scarps may have been modified by human activity: in the point cloud a foot path can be seen along the fault where it crosses the T2-T1 riser. Remote measurements indicated that the crest of the T2-T1 riser is offset left laterally by 6.3 +0.9/–1.3 m (Table 1).

The relationships observed remotely at the site were also reported by an independent field study. Field measurements indicated that the T2-T1 offset was 6.6 m, equivalent within error to that observed remotely (Table 1). However, the remote and field-based observations also showed several differences. In the field, both the T2-T1 and T1-T0 terrace risers were mapped as being left-laterally offset. The T1-T0 riser offset was not inferred from the remote observations due to the strongly embayed and sinusoidal geometry of the riser crest (Fig. 4A). In the field, the fault trace on the T1 surface is defined by an uphill, south-facing escarpment that is 0.2–1.0 m tall. This scarp was not observed remotely. During field work, numerous strands of the fault were found exposed within terrace gravels on the eastern stream bank, with an average strike of 101° and dip of 52°S. Remote observations of such fault exposures were not possible in LiDAR data of this resolution.

### Jameau

The Jameau site (Figs. 2A and 5A–5C) is located inside a meander in the Momance River, where a fluvial terrace (T3) north of the river is cut and displaced by the EPGF. Remote observations indicate that the terrace is ~15 m above the active channel (T0); there are two lower terraces to the west (T2 and T1, Fig. 5A). The western edge of the T3 terrace is displaced by the EPGF, with a T3-T1(?) riser north of the fault and a T3-T2 riser to the south. Remote measurements indicated that the minimum riser offset is 32.2 +1.8/–3.1 m (Table 1). True riser offset was larger if a component of the accumulated lateral offset was removed by lateral erosion of the riser segment north of the fault, as suggested by its proximity to the modern channel and the absence of the T2 terrace. The maximum amount of lateral erosion is constrained by the width of the active channel (~75 m) (e.g., Gold et al., 2009). Therefore, total lateral displacement by the EPGF since formation of the T3 riser ranges from 32 to 106 m. Remote

TABLE 1. COMPILATION OF OFFSET OBSERVATIONS ALONG THE ENRIQUILLO-PLANTAIN GARDEN FAULT, HAITI

Site name	Latitude (°N)	Longitude (°W)	Setting	Offset marker	Remote measurements (this study)		Field measurements	
					Offset (m)	+ error (m)	- error (m)	Offset (m)
Dumay	18.508	72.229	~12 km southeast of Port-au-Prince, ~3.2 km west of Dumay, along a northwest-flowing tributary to the Grise River	T2/T1 fluvial terrace riser	6.3	+0.9	-1.3	6.6
Chauffard (Jameau)	18.477	72.430	~2.4 km northwest of village of Chauffard, where a concave-north meander bend in the Momance River is crossed by the Enriquillo fault	T3/T1–T3/T2 fluvial terrace riser	32.2	+1.8	-3.1	31
Chauffard (Jameau)	18.477	72.430	~2.4 km northwest of village of Chauffard, where a concave-north meander bend in the Momance River is crossed by the Enriquillo fault	shutter ridge, east bank Momance River	27.8	+6.7	-7.2	na
East Chauffard	18.479	72.424	~700 m east of Chauffard site, along a north-flowing tributary on the south side of the Momance River valley	channel deflection	52	+18	-13	na
Fayette (Jean-Jean)	18.472	72.540	~33 km west-southwest of the Dumay site, at the west end of a fluvial terrace that extends for ~0.9 km along the south side of the Momance River	alluvial fan	8.6	+2.8	-2.5	na
Fayette (Jean-Jean)	18.472	72.540	~33 km west-southwest of the Dumay site, at the west end of a fluvial terrace that extends for ~0.9 km along the south side of the Momance River	beheaded gully	14.1	+3.1	-2.4	na

Note: na, indications no data available.

analysis of the site also identified a second, left-lateral displacement of the southeastern wall of the Momance Valley to form a south-facing shutter ridge (Fig. 5C). Horizontal separation of the wall was remotely determined to be 27.8 +6.7/–7.2 m by projecting equivalent topographic contour lines on opposite sides of the fault into the shutter ridge and measuring their separation along the fault trace.

The overall site geometry as observed remotely was also seen in the field, and the riser offset measured in the field (31 m) was equivalent within error to that determined remotely (32.2 +1.8/–3.1 m) (Table 1). However, the field observations also differed from those made remotely. While field observations suggested that there may be a sliver of an abandoned T1(?) terrace surface at the base of the riser north of the fault, this surface was not mapped in the field because it appeared that the riser base is exposed to lateral refreshment by the modern stream during flood events. Although the remote and field-based maps differ in detail, the same conclusion of vulnerability to lateral erosion was also inferred during remote analysis. On the west side of the T3 terrace, the EPGF was found in the field to be clearly exposed in a carbonate bedrock face that defines the east-west-trending slope that separates the faulted riser segments. The fault plane strikes 090° and dips 74°S; slickenlines and mullions on the fault plane rake 37°SW and indicate left-reverse motion. On the east side of the T3 terrace, the fault was clearly evident in a bedrock exposure along the river-bank as a south-dipping fault surface capped by terrace gravels. Such observations of fault exposures were not possible in the LiDAR data set.

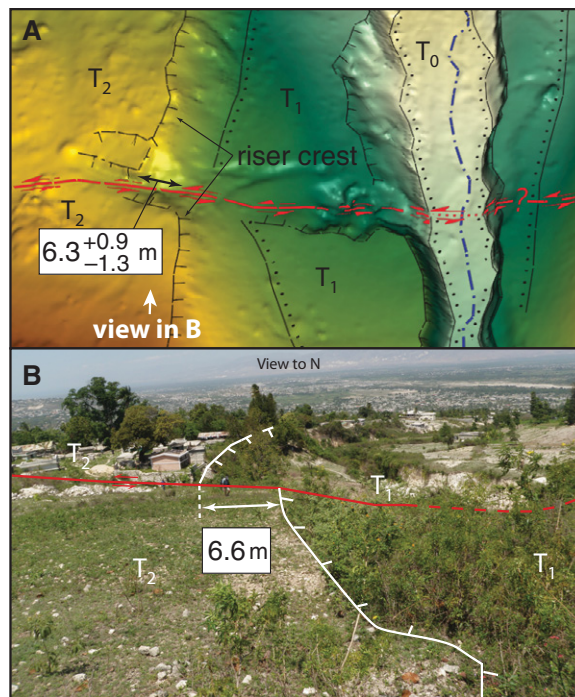
### East Chauffard

A north-flowing tributary ~700 m east of the Jameau site crosses the EPGF along the southern side of the Momance Valley (Figs. 2A and 5D). The thalweg of the tributary is deflected left laterally 52 +18/–13 m where it crosses the fault (Table 1). Although the EPGF is well expressed here, some or all of the channel separation may be due to nontectonic deflection of the stream along the scarp prior to channel incision. The offset (52 m) was determined by measuring the deflection of the thalweg of the tributary channel. The maximum (70 m) and minimum (59 m) offsets were determined by measuring the distances between the outer and inner channel walls, respectively, after projecting them across local deflections at the fault.

### Fayette

Remote observations at the Fayette site (local place name Jean-Jean) suggested an offset alluvial fan and stream channel (Figs. 2A and 6),

**Figure 4.** Comparison of remote and field-based observations at the Dumay site of latest Holocene surface rupture along the Enriquillo–Plantain Garden fault (red). Animation 2 shows use of Crusta software (see text) in an immersive visualization environment to conduct remote neotectonic mapping at this site. (A) Results of our remote analysis. At the site, the topographically expressed trace of the fault is a single strand that displaces the crest of a riser between fluvial terraces T2 and T1 by 6.3 +0.9/−1.3 m on the west bank of a north-flowing channel. The fault is clearly defined by a tectonic furrow and two fault-parallel uphill-facing scarps cutting the T2 terrace. The base digital elevation model (DEM) was produced by manually removing vegetation returns, gridding the point cloud (0.5 m/pixel), and then embedding this higher resolution patch in the DEM (1 m/pixel) generated following automated vegetation removal. (B) Independent field observations confirm results from our remote analysis, including both the existence of a displaced fluvial terrace riser and the magnitude of offset. On both panels, ticked lines denote riser crests, with ticks on the riser face. Lines with dots denote approximate riser bases.



although extensive vegetation cover and anthropogenic modification of the topography here limited confidence in these observations. At the site, the trace of the EPGF is defined by a set of subtle, discontinuous scarps that coincide with the boundary between a fluvial terrace along the Momance River to the north and the base of a steeply sloping valley wall to the south. The valley wall is cut by a north-draining gully. Agricultural terraces 2–4 m high south of the fault have been constructed across the gully and on the valley wall, locally obscuring the fault trace. North of the fault, an alluvial fan ~8–10 m wide appears to have been deposited on top of the fluvial terrace. The fan is evident as arcuate deflections of otherwise linear topographic contours on the gently north sloping surface of the fluvial terrace (Figs. 6B, 6C). The apex of this possible fan is west of the gully, which is the closest potential source, and shows 8.6 +2.8/−2.5 m of left-lateral displacement (Table 1). The gully has incised the eastern edge of the offset fan north of the fault, producing an east-facing scarp. West of the fan apex and north of the fault, a linear channel ~1 m wide appears to be incised into the fluvial terrace. If this channel has been displaced from the same gully south of the fault that is inferred to have generated the

alluvial fan, then it records a displacement of 14.1 +3.1/−2.4 m (Table 1). The fluvial terrace is disrupted by a series of scarps ~25 m north of the EPGF (outside the area shown in Fig. 6) that trend subparallel to both the Momance River and the fault. These scarps are most likely fluvial rather than tectonic in origin, because they consistently face north.

## DISCUSSION

### Comparison of Virtual Reality–Based Analysis with Field Studies

The virtual reality–based method and traditional field-based approaches have complementary strengths, making them both useful during rapid scientific response to major earthquakes. In a traditional field-based effort, such as that following the 3 November 2002  $M_w$  7.9 Denali fault earthquake in Alaska (Haeussler et al., 2004), geologists fly over the fault in an airplane or helicopter to locate the rupture, image the fault using air photos and/or satellite imagery, and then visit the rupture in the field to measure the slip distribution and document the rupture. For comparison, we have described a method for virtual reality–based analysis of LiDAR data

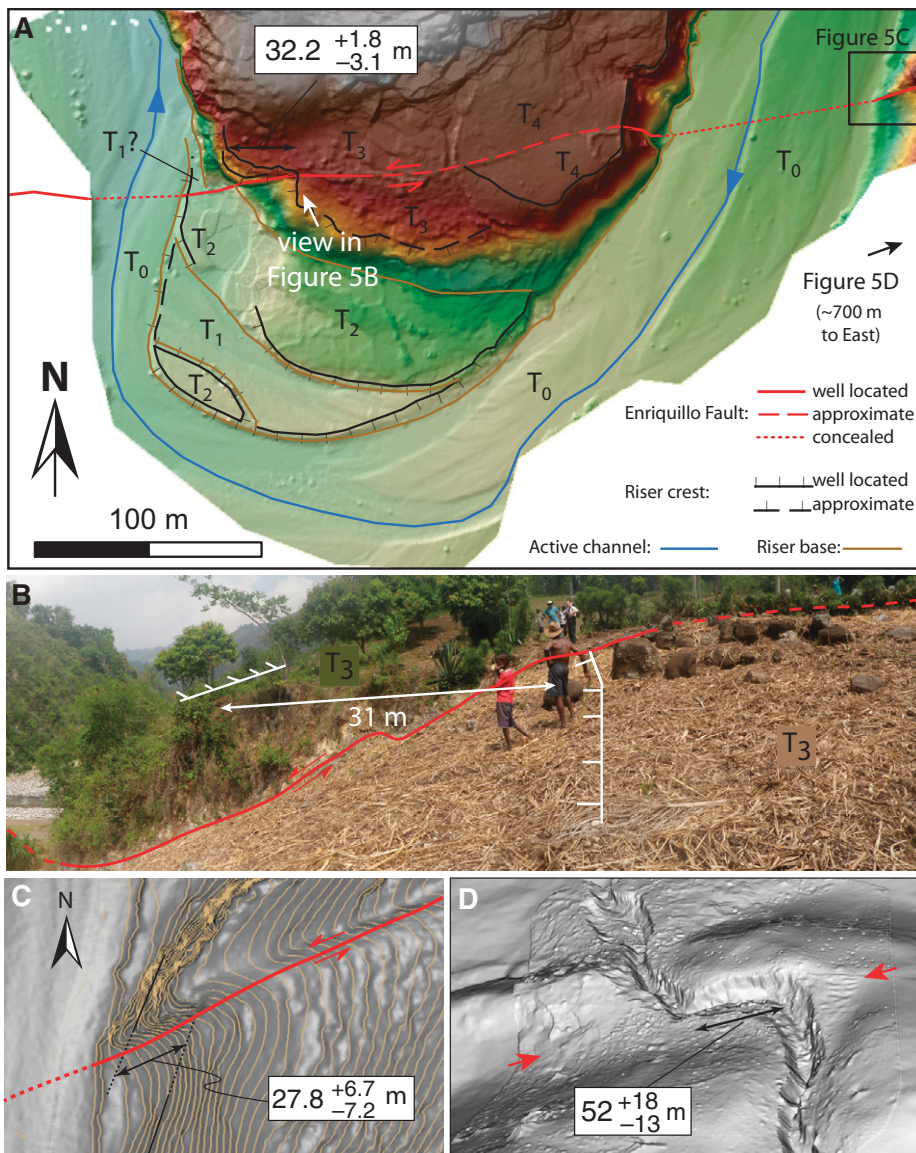
and demonstrated its performance by describing observations it enabled us to make remotely.

Although the Haiti data set is the first large-footprint LiDAR image collected during rapid scientific response to a major earthquake, it did not provide an optimal test for comparing virtual reality– and field-based methods. One problem was the relatively low resolution of the originally released bare-earth DEM. A second was the relatively small number of landform off-sets from ancient earthquakes preserved along the EPGF. The low abundance of well-preserved faulted landforms likely results from a long history of extensive anthropogenic modification of the landscape by deforestation and agricultural activity, which together may have accelerated rates of local erosion and deposition. In addition, relatively low slip rate and high natural rates of surface processes in the tropical setting of Hispaniola likely diminish the lifetime of tectonically generated landforms. The third and most important factor was the absence of surface rupture observed for the 2010 Haiti earthquake (Calais et al., 2002; Hayes et al., 2010; Koehler and Mann, 2011; Prentice et al., 2010), which made it impossible to evaluate the utility of virtual reality–based methods for the rapid discovery and documentation of surface rupture in the context of this earthquake. However, the visualization system described here was also used as part of the analysis of ground-based and airborne LiDAR data collected after the 4 April 2010  $M_w$  7.2 Sierra El Mayor–Cucapah earthquake (Hauksson et al., 2011; Wei et al., 2011), for which there was extensive and complex ground rupture ([http://www.geerassociation.org/GEER\\_Post%20EQ%20Reports/Baja%20California\\_2010/Baja10\\_Ch03.html](http://www.geerassociation.org/GEER_Post%20EQ%20Reports/Baja%20California_2010/Baja10_Ch03.html)) (Oskin et al., 2012). In that event, ground-based LiDAR data were collected days after the rupture, but the airborne data were not acquired for four months, after rapid scientific response efforts were largely complete. Despite the nonideal nature of the Haiti data set, application of a virtual reality–based method of LiDAR analysis did provide a number of insights into the strengths and weaknesses of this approach relative to traditional field-based methods.

### Strengths

The virtual reality method performed better than traditional field-based approaches in several ways.

1. The method provided a rapid synoptic view of the portion of the EPGF imaged by LiDAR. Examination of the data as both point clouds and bare-earth DEMs using real-time, interactive, and immersive data visualization enabled rapid characterization of the regional fault geometry, discovery of two new sites (Dumay, Fayette),



and independent characterization of two others (Jameau and East Chauffard). The virtual reality method also allowed us to easily quantify the 3D geometry of landforms in the LiDAR data. Such measurements, particularly in the vertical direction, may be difficult or impossible with air photos or satellite imagery, due to obscuring vegetation and the subtle vertical expression of some of the offset landforms.

2. The virtual reality method enabled very rapid analysis. Part of this acceleration stemmed from the speed with which we were able to move through the virtual landscape. In addition, the virtual reality method provided unlimited access to the field area. In contrast, field-based studies are often logistically difficult, with significant amounts of time spent getting to and from field sites. They can also be limited by daylight, weather, rugged terrain, and road access or aircraft availability. In the case of the El Mayor–Cucapah earthquake, once the airborne LiDAR data were available, remote mapping of the fault rupture by a 5 member team produced a comprehensive rupture map in ~1 week. This map compared very well with point measurements made in the field over several months, although there were ruptures that were missed on the LiDAR because they were too small or overlooked on the first pass through the data.

3. The virtual reality method posed no risk of interfering with humanitarian efforts in Haiti. Because field-based studies require personnel and logistical support, they have the potential to divert scarce resources away from humanitarian efforts in the damaged area.

4. The visualization tools allowed us to rapidly evaluate the original bare-earth DEM, understand its relationship to the original point measurements, and then rapidly improve the data quality by conducting manual point-cloud classification to identify bare-ground returns in key areas. This capacity is particularly important during rapid scientific response, when time is essential and initial results from automated data processing routines are unlikely to be optimized for fault-related investigation.

5. The virtual reality method enabled us to make accurate measurements of landform offsets. In some cases these appear more accurate than the measurements that can be made in the field during rapid scientific response. Independent field observations at the Dumay and Jameau sites confirmed our site interpretations and offset measurements (Table 1). Interactive manipulation of the terrain view allowed us to iteratively adjust the fit of the piercing line to the landscape and repeat the offset measurements, allowing us to optimize the piercing line projection and check the reproducibility of measurements made from different viewpoints.

**Figure 5.** Offset landforms at Jameau and East Chauffard sites. (A) Surficial geologic map of Jameau obtained via remote analysis in Crusta software (see text). This site is located inside and north of a meander in the Momance River, where a fluvial terrace (T<sub>3</sub>) is cut and displaced by the Enriquillo–Plantain Garden fault. Remote observations indicate that a riser crest on the west edge of the T<sub>3</sub> terrace is displaced at least  $32.2 \pm 1.8 / -3.1$  m. Gridding artifacts are present in the northern part of the digital elevation model (DEM) due to data gaps following removal of vegetation returns. These errors do not affect area in which the riser offset was determined. (B) View to north of riser on western edge of T<sub>3</sub> terrace as seen in the field (photo by R. Gold). The riser offset observed in the field (31 m) is equivalent to that observed remotely. (C) Oblique view from Crusta showing a left-lateral displacement of southeastern wall of the Momance Valley to form a south-facing shutter ridge. Horizontal separation is  $27.8 \pm 6.7 / -7.2$  m, as determined by projecting equivalent topographic contour lines on opposite sides of the fault into the shutter ridge and measuring their separation along the fault trace. Contour lines at 1 m intervals are above arbitrary datum and were generated interactively using Crusta. They appear as bands that color all terrain points that are vertically within  $\pm 5$  cm of the elevation isovalues. These lines can be moved interactively to explore the topography. (D) Remote observations from East Chauffard site. Image from Crusta showing oblique view approximately to the north of a deflected, north-flowing tributary to the Momance River, ~700 m east of Fayette site. Arrows point along fault trace, which is defined by an uphill-facing scarp. The DEMs in A, C, and D were prepared similarly to those in Figure 4.

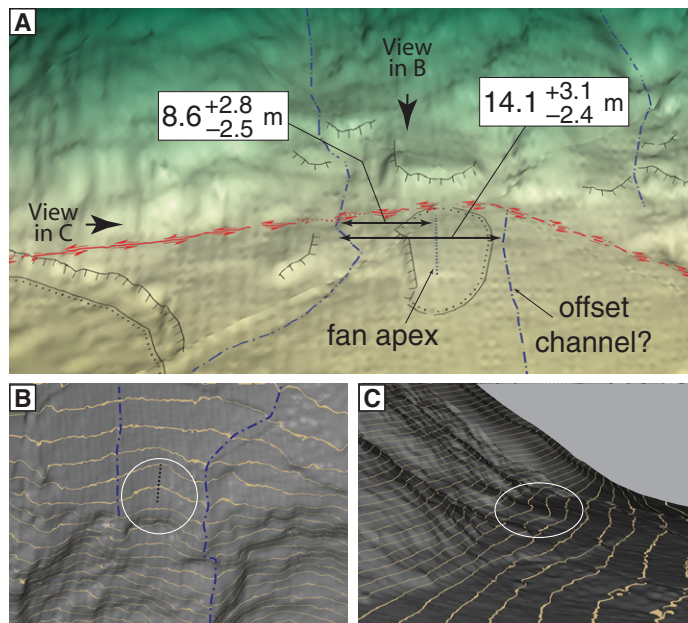


**Figure 6.** Screen shots (i.e., virtual field photographs) from Crusta software showing remote observations of possible landform offsets at the Fayette site, including an alluvial fan and a channel of the fault that appear to have been displaced left laterally by  $8.6 +2.8/-2.5$  m and  $14.1 +3.1/-2.4$  m, respectively, from the closest potential source. (A) Oblique view looking south across trace of the Enriquillo–Plantain Garden fault (red). Black lines with ticks on scarp faces indicate crests of agricultural and erosional scarps. Lines flanked by dots indicate depositional contacts at the margin of an inferred fan and base of a terrace riser. Channel thalwegs are indicated by blue lines with dash-dot pattern. (B) Plan view with 1 m topographic contour lines. White circle outlines deflected contour lines defining possible offset alluvial fan. Note that the crest of the fan is not coincident with drainage to east. (C) Same as B, but viewed obliquely to the west. The digital elevation model was processed as in Figure 4 and contour lines were generated as described in Figure 5.

As a result, we were able to report offsets with uncertainties, whereas the field party did not. In this study and others (Bernardin et al., 2006; Forte et al., 2010) we have found that mapping in a virtual globe environment using the virtual reality method improved feature identification and map accuracy over systems in which mapping can only be done with a plan view of the topography.

#### Weaknesses

In comparison to traditional field-based investigations, the virtual reality–based method showed several important weaknesses.

1. The method was limited by the extent of the data coverage. In the field, it was possible to fly along the fault more or less wherever it went. By contrast, in the virtual reality method, remote observations were not possible in areas not covered by the LiDAR data, such as the

4 km section of the EPGF east of Pétienville that was not imaged. Because a LiDAR survey footprint must be defined from reconnaissance observations (airborne or satellite based), such gaps will arise due to incomplete information at the time of the LiDAR survey.

2. The virtual reality method was also limited by the resolution of the LiDAR data. The point density of LiDAR measurements defined a minimum spatial resolution below which features were difficult or impossible to resolve because they were sampled incompletely or not at all. This threshold limited the size of features that could be resolved remotely and was set by the point density of the original LiDAR measurements, the degree of vegetation cover, and the performance of the automated filtering routine used to obtain the bare-earth model. In case of the Haiti data set, this threshold appears to be  $\sim 3$  m in the horizontal direction. We did

not observe offsets smaller than  $\sim 6$  m, whereas offsets of 1.3–3.3 m were observed in the field (Prentice et al., 2010). However, that level of resolution should be attainable with increased point density and improved point-classification schemes. In the case of the El Mayor–Cucapah data set, which had both a higher resolution point cloud and far less vegetation, the vertical resolution of the LiDAR data was such that the minimum scarp height that could be observed remotely was  $\sim 3$  cm, as compared to a lower limit of  $\sim 1$  cm for scarp heights recorded in the field (Oskin et al., 2012).

3. Because it was not possible to physically touch the landscape using the virtual reality method, this fundamental limitation precluded a number of essential operations, such as identification of rock types, characterization of site stratigraphy, collection of materials for dating, or opening excavations to check soil types or determine the nature of a given depositional unit. Likewise, it was not possible to observe surface roughness or subtle changes in vegetation reflecting changes in underlying rock type. Such field observations would have been particularly useful at the Fayette site, where confidence in the remote observations was compromised by extensive vegetation cover and anthropogenic modification of the topography.

4. It was not possible to observe features exposed in outcrops using the virtual reality method. At both Dumay and Jameau, the field party was able to confirm the location of the fault by checking natural stream exposures. In addition, they were able to make detailed structural measurements to determine the fault orientation and slip directions, observations not possible with virtual reality method.

#### Fault Segmentation and Evidence of Past Surface Rupture

The virtual reality method allowed us to independently reach some of the same first-order conclusions from the 2010 earthquake reached by other studies. These included the remaining seismic hazard to Port-au-Prince (Calais et al., 2010; Hashimoto et al., 2011; Hayes et al., 2010; Mercier de Lèpinay et al., 2011; Prentice et al., 2010), the segmented geometry of the fault (fig. 4 in Calais et al., 2010; Fig. 2B in Prentice et al., 2010), and the anomalous nature of the 2010 event relative to older ruptures (Hayes et al., 2010).

Remote observations reported herein indicated that evidence of ancient surface rupture varies along strike (Figs. 2 and 7). The trace of the EPGF is clear east of Fayette. Likewise, west of Grand Goâve, active faulting is well defined by displaced landforms such as

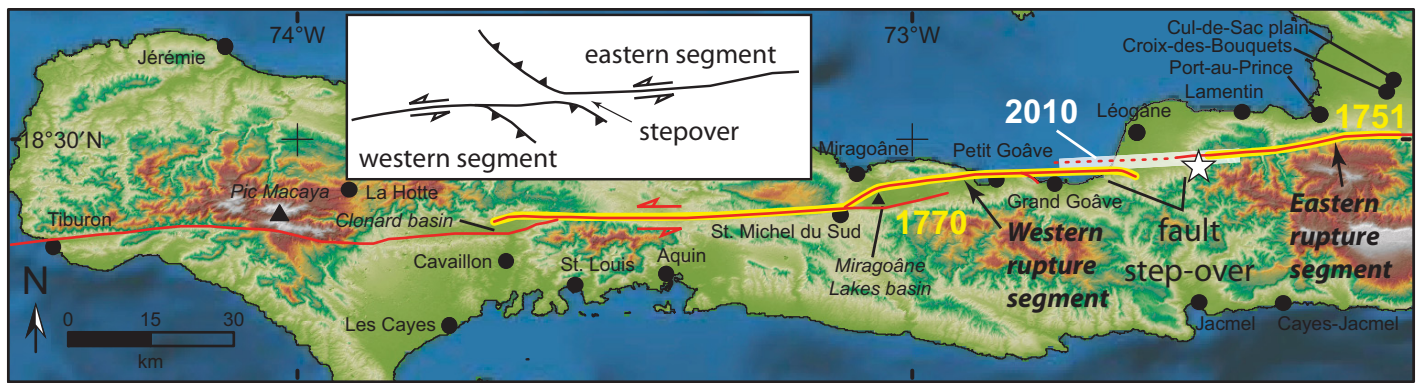


**Figure 7.** Conceptual model of earthquake behavior of the Enriquillo–Plantain Garden fault (red) zone. The 2010 event coincided with an extensional stepover (i.e., transition) between the western and eastern fault reaches, along which the surface expression of active faulting is clear. We propose that these faults are not linked at the surface through the transition, and that this transition defines a boundary between distinct rupture segments with different rupture histories. Earthquake clusters on this segmented fault system may be driven by synchronization of the seismic cycle on the adjacent fault reaches (e.g., Scholz, 2010). Fault rupture pattern (yellow) was reported by Bakun et al. (2012). Inset diagram shows a possible fault pattern reconciling significant reverse slip in 2010 earthquake with the location of rupture in an extensional fault stepover.

uphill-facing scarps at Tapion Du Petit Goâve, although it is not as clear as in the east. Within the intervening transition we found no evidence of ancient surface rupture between L'Acul and the Rouillone River. Thus, we suggest that the eastern and western faults may not be linked at the surface through the transition. We further argue that the transition defines a boundary between distinct rupture segments with different rupture histories.

In detail, we found that the eastern and western fault sections were not aligned along strike, differed in structural style and overall topographic expression, did not show topographic evidence of fault linkage across the surface of the Léogâne fan, and were separated by a region of anomalously embayed range-front topography between Grand Goâve and Fayette. The eastern fault section is broadly linear (Fig. 2A). The prominent topographic expression of the fault and 6–52 m landform offsets here together attest to a protracted record of surface rupture along this reach. This section occurs within steep-walled canyons containing the large, incising Momance and Froide Rivers, and thus is in an area with relatively low potential for preservation of tectonic landforms over several centuries. The preservation of such features attests to their rejuvenation by repeated surface rupture. Independent field observations and image analysis (Prentice et al., 2010) similarly found clear evidence of recent surface rupture in the Momance Valley. Mann et al. (1995) suggested a possible slight transtensional oblique opening along this fault section due to the slight west-southwest strike of the fault here relative to its regional trend. We did not find consistent ver-

tical components of deformation to support this idea, although the fault valley with ~500 m of vertical relief in this segment is the most prominent along the entire EPGF.

In contrast, in the transition west of Fayette, the EPGF projects along strike into the alluvial apron shed from the mountains south of Léogâne (Fig. 2B). There is no evidence of young fault surface ruptures here, despite the high potential for preservation of scarps in the alluvial fans. The trace of the EPGF appears to continue west of Fayette along the sharp range front that defines the southern side of a linear, east-west-trending valley between the Momance and Rouillone Rivers. However, we found no topographic evidence of recent faulting along this front, which we interpret to reflect both westward-decreasing slip rates along this fault segment and extensive modification of the valley floor by agricultural activity and road excavations. Between the Rouillone River and L'Acul, the range front appears to be underlain by a blind, approximately east-striking and south-dipping transpressional thrust or reverse system, as suggested by the ridges at Morne Babou and Morne Diable. These structures likely have a significant component of left slip, due to their low angle of obliquity relative to the overall strike of the EPGF. Reverse or thrust motion is indicated by water and wind gaps and the stream deflection at the eastern end of Morne Diable, all of which suggest that this ridge may be an actively growing fold that likely formed above an obliquely slipping thrust or reverse fault (Figs. 2B, 2E, 2G). At Morne Babou the gorges crossing a stepped range front and ponded sedimentary basins perched above

the Léogâne fan all suggest that this range is above an active, east-striking and south-dipping thrust or reverse fault system. Strike slip within Morne Babou is suggested by elongate, possibly fault-controlled valleys that parallel the overall strike of Morne Babou (Fig. 2B). Koehler and Mann (2011) reported reconnaissance field observations of ponded sediments in closed depressions, beheaded channels, linear valleys, shutter ridges, sidehill benches, and sag ponds within Morne Babou. Slip on the transpressional thrust or reverse system south of Dufort appears to diminish eastward along strike, as suggested by the low relief and strongly embayed range front between Dufort and the Rouillone River. In detail there may be at least two main faults here, one along the northern edge of the foothills and a second ~2 km to the south, at the transition to higher topography (Fig. 2B).

To the west, at Grand Goâve, evidence for recent surface rupture reappears near the terminus of the 2010 rupture as the clear fault with uphill-facing scarps on the southwest side of the ridge at Tapion Du Petit Goâve (Fig. 2F). Reconnaissance field observations also led to the suggestion of probable Holocene faulting along this valley (Prentice et al., 2010) within a possible restraining bend (Koehler and Mann, 2011). Based on our observations alone it is not clear if this fault is a splay off a main trace offshore to the north or the principal trace of the EPGF within a restraining bend; evidence of EPGF-parallel young faults within Grand Goâve Bay (Hornbach et al., 2010) described in the following supports the former interpretation. The ridge at Tapion Du Petit Goâve appears to be an active northeast-vergent fold, based on its

morphology and oblique orientation relative to the overall trace of the EPGF (Fig. 1). Folding is expected in this orientation because it is at a high angle to the maximum shortening direction expected for a zone of sinistral progressive simple shear (e.g., Sylvester, 1988) oriented parallel to the EPGF. The steeper northeast face and symmetric plunge of the ridge crest suggest that the inferred anticline is northeast vergent and doubly plunging. Northwest of Tapion Du Petit Goâve, the elongate ridge north of Port Royal appears to parallel a dominantly left-slip fault that defines the principal trace of the western section of the EPGF in this area. The along-strike variation in elevation and degree of dissection may suggest that this ridge has been progressively uplifted from west to east by a component of north-side-up deformation. The intersection of the eastward projection of this left-slip fault with the northward continuation of Tapion Du Petit Goâve ridge is offshore. The inferred thrust or reverse fault systems at Tapion Du Petit Goâve and between L'Acul and the Rouillone River are likely thrust splays from an offshore continuation of the western fault section to the north. Alternatively, they may be a pair of right-stepping restraining double bends along the principal trace of the EPGF.

Seafloor images derived from multibeam, CHIRP (compressed high intensity radar pulse), and side-scan sonar data collected after the 2010 earthquake imaged scarps and displaced sediments along two traces of the EPGF in Grand Goâve Bay (Hornbach et al., 2010; McHugh et al., 2011). These scarps are located in the southeastern corner of the bay roughly along strike to the west from the fold and thrusts we infer at Morne Babou (Fig. 2B). Based on these scarps and the regional topography, Hornbach et al. (2010) inferred that Tapion Du Petit Goâve is a region of transpression that is flanked by offshore faults along the coastline, and that trans-tension in Petit Goâve Bay changes eastward along strike to transpressional deformation and then strike-slip faulting in the southwestern and southeastern parts of the Grand Goâve Bay, respectively.

Integrating the offshore observations with the structural observations reported here suggests that the ridges at Tapion Du Petit Goâve, Morne Babou, and Morne Diable are folds above thrust splays off the main trace of the EPGF. Although the regional stepover between the western and eastern fault segments is extensional (Fig. 7), it appears that the western fault section may terminate into the transpressional shortening structures at Morne Babou, Morne Diable, and Tapion Du Petit Goâve that are south of both the EPGF and the extensional stepover. Shortening across these structures is consistent with their

oblique, northwest-striking orientation relative to the eastern and western fault sections, which strike northeast. This interpretation differs from that of Prentice et al. (2010), who inferred primarily strike-slip faulting between L'Acul and Fayette.

Aftershocks to the 2010 event are consistent with the interpretation of significant thrusting on either thrust splays or restraining bends at the termination of the western fault segment within the transition zone described herein. In contrast to the mainshock, which was dominantly left slip, nearly all aftershocks were thrust events with nodal planes striking  $\sim$ N120°E and dipping 30°–45° (Mercier de Lèpinay et al., 2011; Nettles and Hjörleifsdóttir, 2010). Based on their spatial distribution, Nettles and Hjörleifsdóttir (2010) interpreted the aftershocks to result from failure of multiple distributed faults and inferred that many of the onshore anticlines are cored by active faults. Mercier de Lèpinay et al. (2011) interpreted the aftershocks as occurring on structures within a northwest-southeast-striking thrust belt that is the along-strike continuation of thrust system in the Muertos trough to the southeast of the EPGF (Fig. 1).

Our inference of a fault stepover between Grand Goâve and Fayette is broadly similar to the fault geometry shown by others. Between Dufort and the Rouillone River, Hornbach et al. (2010) showed a releasing double bend and Koehler and Mann (2011) showed both an extensional step and a subtle bend in the EPGF west of Fayette to a more northward strike. Prentice et al. (2010) noted the lack of evidence for active faulting on the Léogâne fan and also reported that the main fault bends and steps to a more northward strike to follow the range front to the south. Calais et al. (2010, their Fig. 4) showed an extensional step in the EPGF at L'Acul. Mercier de Lèpinay et al. (2011) continued the EPGF trace from Fayette to the tectonic ridge north of Port Royal, well offshore in Grand Goâve Bay; they also showed an extensional stepover between separate western and eastern segments of the EPGF, but placed the step between Miragoâne and Petit Goâve, well west of that inferred here. In their fault model, the western segment of the EPGF terminates into a northeast-directed thrust south of Petit Goâve, with no structures shown at Tapion Du Petit Goâve, Morne Babou, or Morne Diable.

Source models for the 2010 event consistently indicate a significant reverse component on the previously unrecognized north-dipping Léogâne fault (Calais et al., 2010; Hashimoto et al., 2011; Hayes et al., 2010; Mercier de Lèpinay et al., 2011; Nettles and Hjörleifsdóttir, 2010). This is confusing, considering that the regional geometry of the EPGF shows an

overall releasing stepover or bend in the vicinity of the 2010 epicenter. Most studies have remarked on the discordance between motion in the 2010 event and regional topography: in the 2010 event the low area on the Léogâne fan north of the EPGF went up relative to mountainous areas to the south. The explanation for this pattern remains unclear. One possibility is that other faults have produced the topography (Hashimoto et al., 2011), such as the strike-slip linked thrusts south of the western segment of the EPGF inferred above, and that the 2010 event is not representative of long-term deformation in this region. Interference between the EPGF system and the south-directed thrust system to the north has also been proposed (Calais et al., 2010; Mercier de Lèpinay et al., 2011). An alternative possibility is that the eastern segment of the EPGF links with a north-dipping oblique-slip reverse or thrust system, and that the 2010 event reflects slip at this possible termination of the strike-slip segment (Fig. 7).

#### Model of Earthquake Behavior along the EPGF Zone

The remote observations led to a conceptual model for the earthquake behavior of the EPGF that explains both past clustering and the lack of 2010 surface rupture (Fig. 7). Specifically, we suggest that the stepover between Grand Goâve and Fayette divides the fault into separate eastern and western rupture segments. We infer that earthquake clusters on the segmented fault system may be driven by synchronization of the seismic cycle on the adjacent fault reaches (Scholz, 2010) due to stress transfer at the ends of ruptures (Stein, 1999). Within the stepover between the two fault sections, the westward decline of fault expression in the topography broadly mimics the pattern of slip at depth in the 2010 earthquake. Waveform inversions (Hayes et al., 2010; Mercier de Lèpinay et al., 2011) show maximum slip at depth near Fayette, declining abruptly to the east but tapered more gently to the west. We suggest that the poor topographic expression of faulting between Fayette and Tapion Du Petit Goâve (Figs. 1 and 2) may indicate that the location, size, and lack of surface rupture seen in the 2010 event may be common for ruptures along this section of the fault zone. Thus, the 2010 epicentral region appears to occupy a long-lived boundary within the EPGF zone between fault segments that produced larger, surface-rupturing earthquakes (Fig. 7). This interpretation is consistent with modeling results suggesting that smaller earthquakes confined to stepover regions may result from residual stress near the termination of larger, segment-rupturing earthquakes (Duan and Oglesby,

2005). It is also consistent with analysis of historical damage reports indicating that the 1770 and November 1751 events were west and east, respectively, of the 2010 earthquake (Bakun et al., 2012). However, it remains unclear how the dominantly reverse motion of the 2010 event relates to detailed kinematics of deformation within the stepover because the 3D geometry of structures is disputed (Calais et al., 2010; Hashimoto et al., 2011; Hayes et al., 2010; Mercier de Lèpinay et al., 2011; Nettles and Hjørleifsdóttir, 2010), and is not yet fully understood.

### Seismic Hazard for Port-au-Prince

The landform offsets and length of fault showing evidence of repeated past surface rupture further suggest that future earthquakes near Port-au-Prince could be similar or larger in size than the  $M_w$  7.0 of 2010. A similar conclusion was independently reached by Prentice et al. (2010) using different field observations at or near a number of the locations reported here. The landform offsets of 6–8 m at the Dumay and Fayette sites are 33 km apart. We infer that these offsets accumulated over the past ~750–1600 yr, based on the geodetically determined slip rate (Calais et al., 2010; Manaker et al., 2008) and the presence of well-defined uphill-facing scarps in alluvial deposits. Based on their size, these offsets likely record multiple ancient surface-rupturing earthquakes because the independent field observations along the Momance River reported by Prentice et al. (2010) indicate that the most recent event produced 1–3 m of left-lateral surface displacement. We estimate that the probable along-strike extent of past surface ruptures along this fault reach was 40–60 km, based on the observed fault morphology and the distribution of sites where we see 6–8 m offsets. Theoretical relationships using estimated rupture area alone (Hanks and Bakun, 2002) suggest magnitudes for such events of  $M_w$  6.8–7.0. Likewise, mean slip of 2–3 m on a 40–60-km-long rupture would produce a  $M_w$  6.9–7.2 earthquake (Hanks and Kanamori, 1979; Prentice et al., 2010). Thus, an earthquake similar to or larger than the  $M_w$  7.0 2010 event is possible along this portion of the fault. The probability of another large earthquake on the EPGF adjacent to Port-au-Prince should be considered in planning for recovery, a conclusion similarly drawn by Lerner-Lam (2010).

### Implications for Future Rapid Scientific Response

The 12 January 2010 Haiti earthquake was unprecedented in the volume of LiDAR data available within weeks of the rupture, and thus

the opportunity to use those data as part of the rapid scientific response to the event. In this study we attempted to illustrate the depth of insight that can be obtained remotely. Virtual reality analysis of LiDAR data collected following the Haiti and El Mayor–Cucapah earthquakes suggests ways in which virtual reality–based analyses could be integrated with field-based studies to transform future rapid scientific response to major earthquakes and other natural disasters for which LiDAR data are collected.

1. Where possible, use airborne LiDAR to image known and inferred active faults before rupture, as has been done for most major faults in California.

2. Collect a pilot LiDAR image of the fault within days of a major earthquake. Use virtual reality methods to analyze those early results and guide additional data collection and help focus field efforts.

3. Release the LiDAR data to the community within hours or days of collection as they come available, starting with the full point cloud, and then moving to derived data sets, such as the classified cloud and preliminary bare-earth DEMs. When released rapidly, the data are likely to contain errors such as scan misregistration, nonoptimal classification, or gridding artifacts. However, use of advanced visualization tools will enable users to recognize and work around such errors. Because of the need to make observations as quickly as possible, it is more important to release preliminary versions of the data than wait for such errors to be corrected. This philosophy was used very effectively by the Information Products Laboratory for Emergency Response to collect, process, and distribute imagery and LiDAR data following the Haiti earthquake (van Aardt et al., 2011).

4. Compare the pre-event (when available) and post-event data to compute difference maps (e.g., Oskin et al., 2012).

5. Remotely characterize the surface rupture, plan field observations, and compare full and classified clouds to evaluate the preliminary bare-earth DEMs. Share observations openly to support the collective research effort. For example, sharing results of the classification analysis with those generating the DEMs will help refine the classification. Likewise, information on the uncertainties in the bare-earth DEMs is important for those using the data to support field-based or remote mapping.

6. Remotely analyze the bare-earth DEMs to find and map surface rupture and ground-shaking effects such as slumping, liquefaction, or landslides. Provide mapping to other groups, including those mapping in the field, imaging the rupture remotely, performing slip inversions, or deploying seismometers or GPS or geodetic instruments.

7. Use the remote mapping tools to develop a preliminary slip function for the surface rupture (e.g., Quigley et al., 2012). The remote approach may be faster than field-based approaches due to the ability to cover large areas quickly. However, it is also likely to be less accurate than field measurements, due to the lower limit on spatial resolution set by the LiDAR data and the inability to physically interact with the landscape and thereby check offset correlations.

8. Remotely identify key sites for more detailed field investigation, such as locations of maximum slip, areas of distributed deformation or gradients in slip direction, fault sections with low potential for preservation (e.g., stream channels or areas likely to be modified during relief and recovery efforts), or fault junctions or splays.

9. Conduct visual analysis of the full cloud to improve the resolution of the bare-earth DEM by manually classifying small areas of particular importance or to find features not evident in the early release bare-earth DEMs (e.g., small offsets or areas of distributed off-fault deformation).

Such an approach is likely to be most effective if each stage of data collection and analysis during rapid scientific response is done iteratively, with updated versions of each data set being released as the analysis proceeds. Such an approach emulates agile programming methods, such as Evolutionary Software Development or Extreme Programming (<http://www.agiledata.org/essays/evolutionaryDevelopment.html>; <http://www.extremeprogramming.org>; Basili and Turner, 1975; Larman and Basili, 2003; Wood and Kleb, 2002), which emphasize responding to change over following set plans and focusing on rapidly creating working solutions to the most important problems instead of developing more complex global solutions ([agilemanifesto.org](http://agilemanifesto.org)). Such approaches solve problems using self-organizing teams that communicate openly, develop materials iteratively, make frequent small releases, and work in pairs to increase efficiency. Application of such an approach to rapid scientific response would lead to rapidly released, updated, and versioned data sets such as the LiDAR cloud, bare-earth DEM, rupture map, or slip function. Likewise, the development teams would consist of diverse groups of geologists, geophysicists, and computer scientists rather than programmers and their clients. This strategy uses computational thinking (Wing, 2006) to modify the approach used to conduct research during rapid scientific response to major earthquakes. A similar conclusion was reached by van Aardt et al. (2011) based on their experience generating, processing, and distributing data during the rapid response to the Haiti earthquake.

## CONCLUSIONS

The Haiti data set was the first large-footprint airborne LiDAR survey collected within days of a major earthquake. As such, it presented unprecedented opportunities and challenges during the rapid scientific response to this event. By describing the use of an immersive virtual reality environment to analyze these massive amounts of multiresolution terrain data, we have demonstrated the feasibility of conducting remote analysis of LiDAR data during rapid scientific response to natural disasters. Specific conclusions from our study include the following.

1. Advanced methods of virtual reality–based data visualization transform LiDAR data analysis during rapid scientific response. The system we describe here enabled exploration and analysis by supporting virtual field studies in which geologists made remote observations of tectonically produced and modified landforms imaged by LiDAR within hours of its release. The system allowed us to map the overall fault geometry, look for 2010 surface rupture, and identify and document evidence of past surface ruptures by finding, mapping, and measuring landform offsets similar in size to those produced in single large ruptures.

2. The system revealed that the initial vegetation filtering, conducted within days of data collection to enable quick data release, used an aggressive classification scheme that resulted in a bare-earth DEM that was missing topographic detail captured by the full cloud. By conducting manual classification we were able to restore this detail at sites of key landform offsets.

3. Our remote observations of tectonic landforms, range-front morphology, and overall fault geometry suggest that the 2010 rupture coincides with a fault stepover. The fault sections to the west and east of this transition are not aligned along strike, differ in structural style and overall topographic expression, do not show topographic evidence of fault linkage across the surface of the Léogâne fan, and are separated by a region of anomalous range-front topography between Grand Goâve and Fayette.

4. Geomorphic evidence of active faulting within the EPGF zone is clearer east of this stepover than to the west. Between Dumay and Fayette, landform offsets of 6–52 m provide clear evidence of repeated past surface ruptures along this ~35-km-long fault reach, although significant sections of the fault trace have been obscured by the Momance and Froide Rivers and urbanization near Pétionville. The visualization system allowed us to discover two new landform offsets along this reach (Dumay and Fayette) and independently identify two sites that were also found by U.S. Geological Sur-

vey researchers (Jameau and East Chauffard). Our analysis of possible rupture extent and landform offsets indicates that an earthquake similar to or larger than the  $M_w$  7.0 2010 event is possible along the EPGF adjacent to Port-au-Prince.

5. Our remote observations lead to a conceptual model for the earthquake behavior of the EPGF zone that explains both past clustering and the lack of 2010 surface rupture. Specifically, we deduce from the gap of well-defined fault-zone morphology where the 2010 earthquake occurred that this was a relatively small event on a boundary between different rupture segments. In this model, the 2010 earthquake does not repeat historical earthquakes in 1751 or 1770.

6. Our study shows how virtual reality–based data visualization enables many basic aspects of field work to be done remotely, accelerating rapid response, enabling rapid identification of key locations for field investigation, and freeing on-site researchers to focus on collecting data that can only be obtained in the field. We expect that future rapid scientific response will involve real-time integration of such immersive data analysis with essential field-based investigations.

## ACKNOWLEDGMENTS

Supported by National Science Foundation grant OCI-0753407, National Aeronautics and Space Administration grant EOS/03-0663-0306, the W. M. Keck Foundation, and the University of California, Davis. We thank the Rochester Institute of Technology (New York) for the rapid processing and release of LiDAR data. C. Prentice and A. Crone shared field observations in advance of publication and K. Hudnut facilitated LiDAR imaging along the Enriquillo–Plantain Garden fault. Comments on earlier drafts were provided by R. Briggs, M. Rymer, and R. Haugerud, and an anonymous reviewer. We also thank two anonymous reviewers for helpful comments.

## REFERENCES CITED

- Ali, S.T., Freed, A.M., Calais, E., Manaker, D.M., and McCann, W.R., 2008, Coulomb stress evolution in northeastern Caribbean over the past 250 years due to coseismic, postseismic and interseismic deformation: *Geophysical Journal International*, v. 174, p. 904–918, doi:10.1111/j.1365-246X.2008.03634.x.
- Bakun, W.H., Flores, C.H., and ten Brink, U.S., 2012, Significant earthquakes on the Enriquillo fault system, Hispaniola, 1500–2010: Implications for seismic hazard: *Seismological Society of America Bulletin*, v. 102, p. 18–30, doi:10.1785/0120110077.
- Basili, V.R., and Turner, A.J., 1975, Iterative enhancement: a practical technique for software development: *IEEE Transactions on Software Engineering*, v. SE-1, p. 390–396.
- Bernardin, T., Cowgill, E., Gold, R., Hamann, B., Kreylos, O., and Schmitt, A., 2006, Interactive mapping on 3-D terrain models: *Geochemistry Geophysics Geosystems*, v. 7, Q10013, doi:10.1029/2006GC001335.
- Bernardin, T., Cowgill, E., Kreylos, O., Bowles, C., Gold, P., Hamann, B., and Kellogg, L., 2011, Crusta: A new virtual globe for real-time visualization of sub-

- meter digital topography at planetary scales: *Computers & Geosciences*, v. 37, p. 75–85, doi:10.1016/j.cageo.2010.02.006.
- Bilham, R., 2010, Lessons from the Haiti earthquake: *Nature*, v. 463, p. 878–879, doi:10.1038/463878a.
- Bowles, C.J., 2009, Testing classification methods and identifying marine terraces using northern California LiDAR datasets [M.S. thesis]: Davis, University of California Davis, 137 p.
- Calais, E., Mazabraud, Y., Mercier de Lèpinay, B., Mann, P., Mattioli, G., and Jansma, P., 2002, Strain partitioning and fault slip rates in the northeastern Caribbean from GPS measurements: *Geophysical Research Letters*, v. 29, 1856, doi:10.1029/2002GL015397.
- Calais, E., Freed, A.M., Mattioli, G., Amelung, F., Jónsson, S., Jansma, P., Hong, S.-H., Dixon, T., Prépetit, C., and Momplaisir, R., 2010, Transpressional rupture of an unmapped fault during the 2010 Haiti earthquake: *Nature Geoscience*, v. 3, p. 794–799, doi:10.1038/ngeo992.
- Cruz-Neira, C., Sandin, D., DeFanti, T., Kenyon, R., and Hart, J., 1992, The CAVE audio-visual experience automatic virtual environment: *Communications of the ACM*, v. 35, p. 64–72, doi:10.1145/129888.129892.
- DeLong, S.B., Hilley, G.E., Rymer, M.J., and Prentice, C., 2010, Fault zone structure from topography: Signatures of an echelon fault slip at Mustang Ridge on the San Andreas fault, Monterey County, California: *Tectonics*, v. 29, TC5003, doi:10.1029/2010TC002673.
- Dolan, J.F., Mullins, H.T., and Wald, D.J., 1998, Active tectonics of the north-central Caribbean: Oblique collision, strain partitioning, and opposing subducted slabs, *in* Dolan, J.F., and Mann, P., eds., *Active strike-slip and collisional tectonics of the northern Caribbean plate boundary zone*: Geological Society of America Special Paper 326, p. 125–169, doi:10.1130/0-8137-2326-4.1.
- Duan, B., and Oglesby, D.D., 2005, Multicycle dynamics of nonplanar strike-slip faults: *Journal of Geophysical Research*, v. 110, B03304, doi:10.1029/2004JB003298.
- Duan, B., and Oglesby, D.D., 2006, Heterogeneous fault stresses from previous earthquakes and the effect on dynamics of parallel strike-slip faults: *Journal of Geophysical Research*, v. 111, B05309, doi:10.1029/2005JB004138.
- Filin, S., 2004, Surface classification from airborne laser scanning data: *Computers & Geosciences*, v. 30, p. 1033–1041, doi:10.1016/j.cageo.2004.07.009.
- Forte, A.M., Cowgill, E., Bernardin, T., Kreylos, O., and Hamann, B., 2010, Late Cenozoic deformation of the Kura fold-thrust belt, southern Greater Caucasus: *Geological Society of America Bulletin*, v. 122, p. 465–486, doi:10.1130/B26464.1.
- Frankel, K.L., and Dolan, J.F., 2007, Characterizing arid region alluvial fan surface roughness with airborne laser swath mapping digital topographic data: *Journal of Geophysical Research*, v. 112, F02025, doi:10.1029/2006JF000644.
- Frankel, K.L., Brantley, K.S., Dolan, J.F., Finkel, R.C., Klinger, R., Knott, J.R., Machette, M.N., Owen, L.A., Phillips, F.M., Slate, J.L., and Wernicke, B.P., 2007a, Cosmogenic  $^{10}\text{Be}$  and  $^{36}\text{Cl}$  geochronology of offset alluvial fans along the northern Death Valley fault zone: Implications for transient strain in the eastern California shear zone: *Journal of Geophysical Research*, v. 112, B06407, doi:10.1029/2006JB004350.
- Frankel, K.L., Dolan, J.F., Finkel, R.C., Owen, L.A., and Hoeft, J.S., 2007b, Spatial variations in slip rate along the Death Valley–Fish Lake Valley fault system determined from LiDAR topographic data and cosmogenic  $^{10}\text{Be}$  geochronology: *Geophysical Research Letters*, v. 34, L18303, doi:10.1029/2007GL030549.
- Gold, R.D., Cowgill, E., Arrowsmith, J.R., Gosse, J., Chen, X., and Wang, X.F., 2009, Riser diachroneity, lateral erosion, and uncertainty in rates of strike-slip faulting: A case study from Tuzidun along the Altyn Tagh fault, NW China: *Journal of Geophysical Research*, v. 114, B04401, doi:10.1029/2008JB005913.
- Gold, R.D., Cowgill, E., Arrowsmith, J.R., Chen, X., Sharp, W.D., Cooper, K.M., and Wang, X.-F., 2011, Faulted terrace risers place new constraints on the late Quater-

- nary slip rate for the central Altyn Tagh fault, northwest Tibet: *Geological Society of America Bulletin*, v. 123, p. 958–978, doi:10.1130/B30207.1.
- Haeussler, P.J., Schwartz, D.P., Dawson, T.E., Stenner, H.D., Lienkaemper, J.J., Sherrod, B., Cinti, F.R., Montone, P., Craw, P.A., Crone, A.J., and Personius, S.F., 2004, Surface rupture and slip distribution of the Denali and Totschunda faults in the 3 November 2002 M 7.9 earthquake, Alaska: *Seismological Society of America Bulletin*, v. 94, p. S23–S52, doi:10.1785/0120040626.
- Hanks, T.C., and Bakun, W.H., 2002, A bilinear source-scaling model for M-logA observations of continental earthquakes: *Seismological Society of America Bulletin*, v. 92, p. 1841–1846, doi:10.1785/0120010148.
- Hanks, T.C., and Kanamori, H., 1979, A moment magnitude scale: *Journal of Geophysical Research*, v. 84, p. 2348–2350, doi:10.1029/JB084iB05p02348.
- Hashimoto, M., Fukushima, Y., and Fukahata, Y., 2011, Fan-delta uplift and mountain subsidence during the Haiti 2010 earthquake: *Nature Geoscience*, v. 4, p. 255–259, doi:10.1038/ngeo1115.
- Haugerud, R.A., Harding, D.J., Johnson, S.Y., Harless, J.L., Weaver, C.S., and Sherrod, B.L., 2003, High-resolution LiDAR topography of the Puget Lowland, Washington—A bonanza for Earth science: *GSA Today*, v. 13, p. 4–10, doi:10.1130/1052-5173(2003)13<0004:HLTOP>2.0.CO;2.
- Hauksson, E., Stock, J., Hutton, K., Yang, W., Vidal-Villegas, J., and Kanamori, H., 2011, The 2010 M<sub>w</sub> 7.2 El Mayor-Cucapah earthquake sequence, Baja California, Mexico and southernmost California, USA: Active seismotectonics along the Mexican Pacific margin: *Pure and Applied Geophysics*, v. 168, p. 1255–1277, doi:10.1007/s00024-010-0209-7.
- Hayes, G.P., Briggs, R.W., Sladen, A., Fielding, E.J., Prentice, C., Hudnut, K., Mann, P., Taylor, F.W., Crone, A.J., Gold, R.D., Ito, T., and Simons, M., 2010, Complex rupture during the 12 January 2010 Haiti earthquake: *Nature Geoscience*, v. 3, p. 800–805, doi:10.1038/ngeo977.
- Hilley, G.E., DeLong, S., Prentice, C., Blisniuk, K., and Arrowsmith, J.R., 2010, Morphologic dating of fault scarps using airborne laser swath mapping (ALSM) data: *Geophysical Research Letters*, v. 37, L04301, doi:10.1029/2009GL042044.
- Hornbach, M.J., and 20 others, 2010, High tsunami frequency as a result of combined strike-slip faulting and coastal landslides: *Nature Geoscience*, v. 3, p. 783–788, doi:10.1038/ngeo975.
- Ijsselstein, W.A., de Ridder, H., Freeman, J., and Avons, S.E., 2000, Presence: Concept, determinants and measurement, in Rogowitz, B.E., and Pappas, T.N., eds., *Human vision and electronic imaging: Proceedings of the SPIE*, v. 3959, p. 520–529.
- Keller, P., Kreylos, O., Cowgill, E.S., Kellogg, L.H., and Hering-Bertram, M., 2011a, Construction of implicit surfaces from point clouds using a feature-based approach, in Hagen, H., et al., eds., *Scientific Visualization: Interactions, Features, Metaphors: Dagstuhl, Germany, Schloss Dagstuhl—Leibniz Center for Informatics*, p. 129–143, doi:10.4230/DFU.Vol2.SciViz.2011.129.
- Keller, P., Kreylos, O., Vanco, M., Hering-Bertram, M., Cowgill, E.S., Kellogg, L.H., Hamann, B., and Hagen, H., 2011b, Extracting and visualizing structural features in environmental point cloud LiDAR data sets, in Pascucci, V., et al., eds., *Topological methods in data analysis and visualization: Theory, algorithms, and applications: Heidelberg, Germany, Springer-Verlag*, p. 179–192.
- King, G.C.P., and Nabelek, J.F., 1985, Role of fault bends in the initiation and termination of earthquake rupture: *Science*, v. 228, p. 984–987, doi:10.1126/science.228.4702.984.
- Koehler, R.D., and Mann, P., 2011, Field observations from the January 12, 2010, Haiti earthquake: Implications for seismic hazards and future post-earthquake reconnaissance investigations in Alaska: *Alaska Division of Geological and Geophysical Surveys Report of Investigation 2011–2*, 24 p., <http://www.dggs.alaska.gov/pubs/id/22462>.
- Kovač, B., and Žalik, B., 2010, Visualization of LIDAR datasets using point-based rendering technique: *Computers & Geosciences*, v. 36, p. 1443–1450, doi:10.1016/j.cageo.2010.02.011.
- Kreylos, O., 2008, Environment-independent VR development, in *Bebis, G., et al., eds., Advances in Visual Computing, ISVC 2008, Part I, Volume 5358/2008: Lecture Notes in Computer Science: Berlin, Heidelberg, Springer-Verlag*, p. 901–912.
- Kreylos, O., Bethel, E.W., Ligocki, T.J., and Hamann, B., 2003, Virtual-reality based interactive exploration of multiresolution data, in *Farin, G., et al., eds., Hierarchical and geometrical methods in scientific visualization: Heidelberg, Germany, Springer-Verlag*, p. 205–224.
- Kreylos, O., Bawden, G., and Kellogg, L., 2008, Immersive visualization and analysis of LiDAR data, in *Bebis, G., et al., eds., Advances in Visual Computing, ISVC 2008, Part I, Volume 5358/2008: Lecture Notes in Computer Science: Berlin, Heidelberg, Springer-Verlag*, p. 846–855.
- Larman, C., and Basili, V.R., 2003, Iterative and incremental development: A brief history: *IEEE Computer*, v. 36, p. 47–56, doi:10.1109/MC.2003.1204375.
- Lerner-Lam, A.L., 2010, Beyond bricks and mortar: *Nature Geoscience*, v. 3, p. 740–741, doi:10.1038/ngeo1003.
- Lombard, M., and Ditton, T., 1997, At the heart of it all: The concept of presence: *Journal of Computer-Mediated Communication*, v. 3, no. 2, <http://jcmc.indiana.edu/vol3/issue2/lombard.html>.
- Lozos, J.C., Oglesby, D.D., Duan, B., and Wesnousky, S.G., 2011, The effects of double fault bends on rupture propagation: A geometrical parameter study: *Seismological Society of America Bulletin*, v. 101, p. 385–398, doi:10.1785/0120100029.
- Manaker, D.M., Calais, E., Freed, A.M., Ali, S.T., Przybyski, P., Mattioli, G., Jansma, P., Prèpetit, C., and de Chabalière, J.B., 2008, Interseismic plate coupling and strain partitioning in the northeastern Caribbean: *Geophysical Journal International*, v. 174, p. 889–903, doi:10.1111/j.1365-246X.2008.03819.x.
- Mann, P., Taylor, F.W., Edwards, R.L., and Ku, T.L., 1995, Actively evolving microplate formation by oblique collision and sideways motion along strike-slip faults: An example from the northeastern Caribbean plate margin: *Tectonophysics*, v. 246, p. 1–69, doi:10.1016/0040-1951(94)00268-E.
- Mann, P., Prentice, C.S., Burr, G., Peña, L.R., and Taylor, F.W., 1998, Tectonic geomorphology and paleoseismology of the Septentrional fault system, Dominican Republic, in *Dolan, J.F., and Mann, P., eds., Active strike-slip and collisional tectonics of the northern Caribbean plate boundary zone: Geological Society of America Special Paper 326*, p. 63–123, doi:10.1130/0-8137-2326-4.63.
- Mann, P., Calais, E., Ruegg, J.-C., DeMets, C., Jansma, P.E., and Mattioli, G.S., 2002, Oblique collision in the northeastern Caribbean from GPS measurements and geological observations: *Tectonics*, v. 21, 1057, doi:10.1029/2001TC001304.
- McCann, W.R., 2006, Estimating the threat of tsunamigenic earthquakes and earthquake induced landslide tsunami in the Caribbean, in *Mercado-Irizarry, A., and Liu, P., eds., Caribbean tsunami hazard: Singapore, World Scientific Publishing Co.*, p. 43–65.
- McGreevy, M.W., 1992, The presence of field geologists in Mars-like terrain: Presence: *Teleoperators and Virtual Environments*, v. 1, p. 375–403.
- McHugh, C.M., and 15 others, 2011, Offshore sedimentary effects of the 12 January 2010 Haiti earthquake: *Geology*, v. 39, p. 723–726, doi:10.1130/G31815.1.
- Mercier de Lépinay, B., and 15 others, 2011, The 2010 Haiti earthquake: A complex fault pattern constrained by seismologic and tectonic observations: *Geophysical Research Letters*, v. 38, L22305, doi:10.1029/2011GL049799.
- Minski, M., 1980, *TelePresence: Omni*, June, p. 45–51.
- Nettles, M., and Hjörleifsdóttir, V., 2010, Earthquake source parameters for the 2010 January Haiti main shock and aftershock sequence: *Geophysical Journal International*, v. 183, p. 375–380, doi:10.1111/j.1365-246X.2010.04732.x.
- Oglesby, D.D., 2005, The dynamics of strike-slip step-overs with linking dip-slip faults: *Seismological Society of America Bulletin*, v. 95, p. 1604–1622, doi:10.1785/0120050058.
- Oskin, M., Le, K., and Strane, M.D., 2007a, Quantifying fault-zone activity in arid environments with high-resolution topography: *Geophysical Research Letters*, v. 34, L23S05, doi:10.1029/2007GL031295.
- Oskin, M., Perg, L., Blumentritt, D., Mukhopadhyay, S., and Iriondo, A., 2007b, Slip rate of the Calico fault: Implications for geologic vs. geodetic rate discrepancy in the Eastern California Shear Zone: *Journal of Geophysical Research*, v. 112, B03402, doi:10.1029/2006JB004451.
- Oskin, M.E., Arrowsmith, J.R., Corona, A.H., Elliott, A.J., Fletcher, J.M., Fielding, E.J., Gold, P.O., Garcia, J.J.G., Hudnut, K.W., Liu-Zeng, J., and Teran, O.J., 2012, Near-field deformation from the El Mayor–Cucapah earthquake revealed by differential LiDAR: *Science*, v. 335, p. 702–705, doi:10.1126/science.1213778.
- Prentice, C.S., Mann, P., Crone, A.J., Gold, R.D., Hudnut, K.W., Briggs, R.W., Koehler, R.D., and Jean, P., 2010, Seismic hazard of the Enriquillo-Plantain Garden fault in Haiti inferred from palaeoseismology: *Nature Geoscience*, v. 3, p. 789–793, doi:10.1038/ngeo991.
- Quigley, M., Van Dissen, R., Litchfield, N., Villamor, P., Duffy, B., Barrell, D., Furlong, K., Stahl, T., Bilderback, E., and Noble, D., 2012, Surface rupture during the 2010 M<sub>w</sub> 7.1 Darfield (Canterbury) earthquake: Implications for fault rupture dynamics and seismic-hazard analysis: *Geology*, v. 40, p. 55–58, doi:10.1130/G32528.1.
- Scherer, J., 1912, Great earthquakes in the Island of Haiti: *Seismological Society of America Bulletin*, v. 2, p. 161–180.
- Scholz, C.H., 2010, Large earthquake triggering, clustering, and synchronization of faults: *Seismological Society of America Bulletin*, v. 100, p. 901–909, doi:10.1785/0120090309.
- Segall, P., and Pollard, D.D., 1980, Mechanics of discontinuous faults: *Journal of Geophysical Research*, v. 85, p. 4337–4350, doi:10.1029/JB085iB08p04337.
- Stein, R.S., 1999, The role of stress transfer in earthquake occurrence: *Nature*, v. 402, p. 605–609, doi:10.1038/45144.
- Steuer, J., 1995, Defining virtual reality: Dimensions determining telepresence, in *Biocca, F., and Levy, M.R., eds., Communication in the age of virtual reality: Hillsdale, New Jersey, Lawrence Erlbaum Associates*, p. 33–56.
- Stockli, R., Vermote, E., Saleous, N., Simmon, R., and Hering, D., 2006, True color Earth data set includes seasonal dynamics: *Eos (Transactions, American Geophysical Union)*, v. 87, p. 49, doi:10.1029/2006EO050002.
- Sylvester, A., 1988, Strike-slip faults: *Geological Society of America Bulletin*, v. 100, p. 1666–1703, doi:10.1130/0016-7606(1988)100<1666:SSF>2.3.CO;2.
- U.S. Army Map Service, 1962, *Fond Ferrier, edition 2-AMS, series E732, sheet 5771 III: Washington, D.C., National Imagery and Mapping Agency, scale 1:50,000*, <http://www.lib.utexas.edu/maps/topo/haiti/>.
- U.S. Army Map Service, 1988, *Petit-Goâve, edition 3-DMA, series E732, sheet 5671 III: Washington, D.C., National Imagery and Mapping Agency, scale 1:50,000*, <http://www.lib.utexas.edu/maps/topo/haiti/>.
- U.S. Army Map Service, 1991a, *Croix des Bouquets, edition 2-DMA, series E732, sheet 5771 I: Washington, D.C., National Imagery and Mapping Agency, scale 1:50,000*, <http://www.lib.utexas.edu/maps/topo/haiti/>.
- U.S. Army Map Service, 1991b, *Trouin, edition 3-DMA, series E732, sheet 5671 II: Washington, D.C., National Imagery and Mapping Agency, scale 1:50,000*, <http://www.lib.utexas.edu/maps/topo/haiti/>.
- van Aardt, J.A.N., and 15 others, 2011, Geospatial disaster response during the Haiti earthquake: A case study spanning airborne deployment, data collection, transfer, processing, and dissemination: *Photogrammetric Engineering and Remote Sensing*, v. 77, p. 943–952.
- Wei, S., Fielding, E., Prentice, S., Sladen, A., Avouac, J.-P., Helmberger, D., Hauksson, E., Chu, R., Simons, M., Hudnut, K., Hering, T., and Briggs, R., 2011, Superficial simplicity of the 2010 El Mayor–Cucapah earthquake of Baja California in Mexico: *Nature Geoscience*, v. 4, p. 615–618, doi:10.1038/ngeo1213.

- Wesnousky, S.G., 1988, Seismological and structural evolution of strike-slip faults: *Nature*, v. 335, p. 340–343, doi:10.1038/335340a0.
- Wesnousky, S.G., 2006, Predicting the endpoints of earthquake ruptures: *Nature*, v. 444, p. 358–360, doi:10.1038/nature05275.
- Wing, J.M., 2006, Computational thinking: *Communications of the ACM*, v. 49, p. 33–35, doi:10.1145/1118178.1118215.
- Wirth, W., and 14 others, 2007, A process model of the formation of spatial presence experiences: *Media Psychology*, v. 9, p. 493–525, doi:10.1080/15213260701283079.
- Witmer, B.G., and Singer, M.J., 1998, Measuring presence in virtual environments: A presence questionnaire: *Presence: Teleoperators and Virtual Environments*, v. 7, p. 225–240, doi:10.1162/105474698565686.
- Wood, W.A., and Kleb, W.L., 2002, Extreme programming in a research environment, *in* Wells, D., and Williams, L., eds., *Extreme programming and agile methods—XP/Agile Universe 2002; Second XP Universe and First Agile Universe Conference*, Volume 2418: *Lecture Notes in Computer Science*: Berlin, Heidelberg, Springer-Verlag, p. 89–99.
- Zielke, O., Arrowsmith, J.R., Ludwig, L.G., and Akciz, S.O., 2010, Slip in the 1857 and earlier large earthquakes along the Carrizo Plain, San Andreas fault: *Science*, v. 327, p. 1119–1122, doi:10.1126/science.1182781.

MANUSCRIPT RECEIVED 16 MARCH 2011

REVISED MANUSCRIPT RECEIVED 16 FEBRUARY 2012

MANUSCRIPT ACCEPTED 17 FEBRUARY 2012